FACULTY
OF SCIENCE

Prototyping of an automated cyclic Neutron Activation Analysis setup

Cornelius Maurer

Thesis submitted for the degree of Master of Science
Project duration: 8 months

Supervised by Robert J. W. Frost and Kristina Eriksson-Stenström

Department of Physics
Division of Nuclear Physics

May 2022

Abstract

A prototype Neutron Activation Analysis (NAA) setup based on a Deuterium-Tritium (DT) neutron generator is under development at Lund University. It serves as proof-of-principle for NAA based on a Compact Accelerator-driven Neutron Source. One purpose of the setup is to test the possibility of providing environmental monitoring of pure alpha-emitters for the European Spallation Source currently under construction outside of Lund. As availability of reactor-based NAA is in decline within the European Union, alternative sources of neutrons are of great value. The DT-generator used in the current setup has a neutron yield of $\sim 10^8$ n/s. The setup uses a fast pneumatic sample-transport system, which provides capabilities for measuring activation product half-lives in the sub-second range, and two HPGe detectors for gamma-ray spectroscopy providing the option of gamma-gamma coincidence measurements. In recent work, a Programmable Logic Controller-operated pneumatic- and data acquisition system, as well as new sample holders were implemented. This report provides an overview of the implemented improvements, as well as demonstration measurements for the different analysis types that can be performed with this setup. Samples measured include In, NaCl, Gd_2O_3 and soil samples from the surroundings of the ESS building grounds. The most important results feature a working automated cyclic-NAA prototype, with the capability of measuring samples with half-lives down to the sub-second region (transport time from irradiation to detectors of 350 ms). For pure samples the detection limits can currently reach down to the order of sub-mg while using a neutron generator with an output of only $4.7*10^8$ n/s. The setup also features the capabilities to investigate the half-life of the desired lines, as well as coincidence measurements on samples where this technique is applicable. In order to get to the state of monitoring environmental samples, more work is needed to significantly push down detection limits in the future. This could include coincidence measurements, improved background subtraction and measuring samples with known mixed composition.

Contents

List of figures **vii**

List of tables **ix**

List of abbreviations **x**

List of other works produced in relation to this project **xi**

1 Introduction **1**

1.1 Motivation 1

1.1.1 Aims 2

1.2 Background 3

1.3 Report structure 3

2 Theory **4**

2.1 Nuclear phenomena 4

2.1.1 Nuclear structure 4

2.1.2 Nuclear reactions 5

2.1.3 Cross-sections 5

2.2 Processes within NAA 5

2.2.1 Neutron activation 5

2.2.2 Gamma ray interaction with matter 7

3 System Development **8**

3.1 Initial configuration and upgrade potential 8

3.2 Implemented upgrades 9

3.2.1 New sample holder 9

3.2.2 PLC control system 9
3.2.3 Pressure system 10
3.2.4 The data acquisition system 14

4 Experimental procedures and data analysis 16
4.1 Measurements 16
4.1.1 Energy and efficiency calibration 16
4.1.2 Background measurement 16
4.1.3 Signal-to-background-ratio 17
4.1.4 Sample measurements 18
4.2 Data analysis 18
4.2.1 Energy and efficiency calibration 19
4.2.2 Dead-time estimation 22
4.2.3 Noise level analysis 24
4.2.4 Background correction 24
4.2.5 Signal-to-background-ratio 24
4.2.6 Decay analysis 25
4.2.7 Coincidence analysis 25

5 Results 26
5.1 Determination of setup parameters 26
5.1.1 Background determination 26
5.1.2 Noise level determination 26
5.1.3 Signal-to-background ratio study 27
5.2 Different measurement types 32
5.2.1 Spectral analysis 32
5.2.2 Decay study 34
5.2.3 Coincidence analysis 35

6 Discussion 36
6.1 Setup characterisations 36
6.1.1 Energy and efficiency calibration 36
6.1.2 Dead-time correction 36

6.1.3 Channel noise . . . 37
6.1.4 Background measurement . . . 37
6.1.5 SBR-measurements . . . 38
6.2 Measurements . . . 38
6.2.1 Decay analysis . . . 39
6.2.2 Coincidence analysis . . . 39
6.2.3 Spectral analysis . . . 39

7 Summary and outlook **41**
7.1 Conclusions . . . 41
7.2 Future work . . . 42

Acknowledgements **42**

References **43**

Appendices

A Table of observable reactions within the used samples **48**

B Table of peaks fitted in the sample spectra. **53**

List of Figures

2.1 Graph demonstrating the behaviour of a saturation process common on NAA. Over the course of 5 half-lives the curve reaches a point very close to saturation. 6

3.1 Work principle of the NAA-setup. The sample is transported between source and detectors by the pneumatic transport line. 8

3.2 Schematic of the four valves that were used in the initial setup. Two of the valves would each form complementary sets, one opening the line on one end to surrounding air, while the other would open the line to the lab's 7 bar pressure supply line. 9

3.3 The original design of the sample holder. The inner volume is 6.616 cm^3 (later version changed to 4.67 cm^3). Edges at top and bottom are rounded to reduce the probability to get stuck in the tube. The software Fusion360 [31] was used to generate the figure. 10

3.4 Capture of the visualisation window from TcXAEShell [33]. It shows the input and control fields for the time setting for the cycles, as well as status indication lights, a button for starting the measurement and a Kill switch killing all output signals. 12

3.5 Circuit diagram for the PLC system. The Beckhoff modules control the pneumatic line valves and trigger acquisition on the MCA by gating for active acquisition. There is also the possibility to read in a control signal from the generator, as well as giving a start signal to the generator. 12

3.6 Diagram for the pneumatic system. The two 5/3-way valves are controlled by the PLC system sketched in Fig. 3.5. 13

3.7 Sketch of the designed detector guide. It fixes the two end caps of the HPGe detectors and provides horizontal alignment for the steel tube containing the sample containers. Design and rendering done with Fusion360 [31]. 14

4.1 Gamma-ray spectrum for the ^{152}Eu-source used for energy calibration. The plot shows the fits for the lines which are above 5% relative intensity. The energy calibration consists of a linear fit of the corresponding energy to the 16384 bins within the recorded spectrum. 20

4.2 Efficiency curve of the two detectors. The data combines ^{152}Eu and ^{226}Ra data combined by normalising to the efficiency for ^{60}Co at 1332 keV. The fit is performed using Eq. (4.1). It is important to note that this is not viable as absolute efficiency measure, due to the uncertainty in the source activities. Uncertainties plotted are based only on Poisson-statistics of the counts within the fitted peaks. Using a calibrated source or the external-trigger method ([37]) would be able to provide this though. According to the manufacturer, the relative efficiency of these detectors is ∼20%, and although the measurements here are not taken at 25 cm distance, it still seems like the estimation could be a little bit too high here. This should be fixed using either of the proposed methods. 21

4.3 Demonstration of the deadtime estimation produced by the programmed algorithm (OWN), against the intrinsic dead-time estimation performed by COMPASS itself. Here a) shows the full range, while b) is zoomed in to the lower end of the data. The black line indicates the line of equality. The relation seems to be linear, except for the two measurements that show up underneath the equality line. This is discussed in Section 6.1.2. For this purpose a wide range of sources was used, some with different distances between detector and source (indicated by numbering) in order to get a wider range of dead-times. The isotopes used were ^{24}Na, ^{55}Fe, ^{60}Co, ^{152}Eu, ^{226}Ra and ^{252}Cf, plus one measurement without any source (BG). 23

5.1 Three spectra from the background measurement, all taken from a 30 min time slice. Spectrum A is taken while the generator is still running, the other two are the two 30 min slices thereafter. 27

5.2 Plot of the determined noise (the difference between the two different summations of the background spectra, in 30 s alternates) and the exponential fit to the data retrieved by fitting an exponential decay to the absolute value multiplied by a factor of 3 after rebinning the data by a factor of 128. The fit results are listed in Tab. 5.1. 28

5.3 Results of the SBR-study. For this, the Indium sample was run with different time sets: Both for 10 and 5 half-lives measurements were taken with measurement intervals being multiples of the 162 keV line half-life of 2.2 s. After measuring the samples were set to cool down at the detector end until the sum of measurement and cooldown time reached the sum of 10 half-lives (i.e. 22 s), reaching a negligible level of activity of this line. While the signal in b) seems to follow a saturation, at least the lower end in a) indicate a fairly linear relation most likely due to the linear background. The point with the best SBR is thus reached when measuring for only one half-life. 30

5.4 The same three figures as presented in Fig. 5.3, only that now generator background subtraction was performed on this set. There is a clear difference in the amount of background counts, here only originating in the Compton continuum part of the higher-energy lines. 31

5.5 Three exemplary Background subtracted gamma spectra for In, Hf and Steel. The peaks that could be associated to lines from the different isotopes produced in the NAA are labeled, more information on the fit to the peaks can be found in Table B.1. The spectra are all taken from Detector 1. 33

5.6 Counts within an energy window of 162±2 keV accumulating over a time window of 110 ms summed over all and the exponential fit to this data. The fit coefficients are $\beta = 2.012 \pm 0.0025$ s for the half-life and $A = 257 \pm 16$ counts for the activation factor. 34

5.7 Coincidence analysis of a ^{60}Co-spectrum. The time window used was 500 ns. 35

List of Tables

3.1 Results from the PIXE-analysis of the PLA used in the sample holders [32]. Specifically interesting are abundances of elements with a Z equal to or higher than Silicon (Z=14). The isotopes that were found, based on simulations [17], do not need to be considered in the analysis. The concentration is given with the uncertainty in parentheses. 11

3.2 Settings within the COMPASS software configuring ADC conversion and charge integration. For the threshold, lsb stands for least significant bit. . . . 15

3.3 Settings within the COMPASS software configuring the MCA Board (DT5780, CAEN) coincidence settings. These were used to gate the acquisition with the PLC control system using a TTL signal fed into the Trig In port at the board. 15

4.1 Measurements for the SNR-study. The line that was studied in particular is the 162 keV-line from ^{116m2}In. All measurements were run for at least 30 cycles, whereas for evaluation sets with more cycles were reduced to 30 for comparability. The base time used for all the measurements was 2.2 s, the corresponding half-life of this line. The irradiation and measurement columns list the multiple of the half-life that was used (unit of half-life, [hl]). The cooldown is given either in [hl] or seconds, depending on which was applicable. The weight is given with the uncertainty in parentheses. 17

4.2 Details of samples measured. The table lists the sample composition as well as the half-life of interest (listed as base time). This gives the base time for the factors for irradiation and measurement times. The cooldown is given either as multiple of the half-life (without units), or as the time in seconds, as for very short half-lives the cooldown was stretched out for the sake of the vacuum system to recuperate. 18

4.3 Results from the PIXE-analysis of the steel bolt. Comparing with Table A.1 and the results in Fig. 5.5c, the interesting reactions within the sample are mostly ^{56}Fe(n,γ)^{56}Mn, ^{55}Mn(n,γ)^{56}Mn, and ^{27}Al(n,γ)^{28}Al. Results provided by [32]. 19

5.1 Fit coefficients of the exponential function for the noise within the two channels. 27

5.2 Detection limits for the different elements. The values were determined by assuming a linear correlation between sample mass and signal strength, and then scaling the peak towards the noise level, to find the point where the it will stand out against background (see Eq. (5.3)). The masses were corrected by percentage of weight within the compounds. This means the detection limit gives the minimal total mass of the element (within a sample) needed for detection. 34

A.1 Table of delayed gamma emission after neutron activation. Compiled from: [42, 43] (reaction and abundance), the ENSDF library via [41](half-life, lines and rel. intensity) and the ENDF/B VIII.0 dataset [44] (cross-sections) . . . 48

B.1 Table of the fitted peaks within the background-corrected spectra. 53

B.1 Table of the fitted peaks within the background-corrected spectra. 54

B.1 Table of the fitted peaks within the background-corrected spectra. 55

List of Abbreviations

CANS	Compact Accelerator-based Neutron Source
DC	Direct current
DT	Deuterium-Tritium
DAQ	data-acquisition
FWHM	Full-width at half-maximum
HPGe	high-purity germanium
hl	half-life (used as unit)
MCA	multi-channel analyzer
MC	Monte-Carlo
NAA	Neutron Activation Analysis
PLA	Polylactic Acid
ppm	parts per million
PIXE	Proton induced X-ray emission
PLC	Programmable Logic Control
SBR	Signal-to-background ratio

List of other works produced in relation to this project

The prototyping of a high-resolution neutron activation analysis system - based on a Pelletron accelerator and fast pneumatic sample-transport, Authors: R. J.W. Frost and M. Elfman and P. Kristiansson and J. Lindsey-Clark and C. Maurer and J. Pallon and G. Pedehontaa-Hiaa

Under Review

1 Introduction

Neutron Activation Analysis (NAA) is a method where a sample can be analysed for isotopic composition using a neutron source and a measurement procedure named gamma spectroscopy. For this purpose the sample is first "activated" by irrradiation using the neutron source, classically a nuclear reactor, and then transported to a detector setup where the characteristic gamma spectrum that the sample emits can be analysed. When dealing with low concentrations, it can often be of value to perform more than one measurement with the same sample to increase statistics. This is then called cyclic-NAA and is the main topic of this work.

To give an idea of the capabilities of NAA, a few scientific applications of NAA should be mentioned here. The review of Witkowska from 2004 [1] discusses NAA as valuable tool in the analysis of several different human samples, as well as in various different use cases of environmental analysis. NAA has also been used to investigate geological and archaeological studies [2, 3]. NAA may also be used as means of analysing the content of suspicious or closed off cargo containers to quickly evaluate potentially dangerous freight or fissionable material [4, 5]. This work focuses on using NAA as means to perform analysis of short-lived activation products and environmental samples.

At the Division of Nuclear Physics at Lund University, INAA ICS (Iridium coincidence spectrometry) has been used before, however with a different detector setup. It was part of surveys providing important geological data [2, 6]. A disadvantage of the ICS setup is that it relies on the sample being transported to a fission reactor for irradiation. The desire to remove the dependence on off-site irradiation of sample has motivated a new project [7, 8] , to construct a compact accelerator-driven neutron source (CANS). This CANS will provide neutrons for a new NAA system. The development of a smaller prototype NAA system has begun, using a DT-neutron generator [9]. This development is now to be continued within this work.

1.1 Motivation

The European Spallation Source (ESS) will generate more than 1000 different radionuclides [10]. Some of those will be released into the environment during normal operation, while others will be released specifically in the case of an accident. To control the dose rate the public is exposed to, precise and locally available methods of quantifying these radionuclides are of utmost importance. The setup, which is the subject of this work, has been developed to apply the NAA technique to observe small concentrations of isotopes within other samples. The ultimate goal is to determine the utility of the setup for measuring ^{148}Gd as prime example, one of the most important isotopes emitted by ESS, when examining soil or air samples [11]. This work will advance previous work [9] on the path towards that goal, focusing mainly on automating the measurement process. The importance here is given by ^{148}Gd being a pure alpha emitter, which cannot be detected by conventional gamma or beta radiation detectors [10]. Moreover, the inhalation and ingestion of ^{148}Gd is believed

to be one of the major sources of radiation dose to the public in case of an accident, if activated material from the tungsten target ESS would be released into the environment. Alpha emitters are not as harmful when outside of the body, as they only have a short range when travelling in air, and moreover will also be stopped by the outer layer of dead cells on top of the skin. Once inside the body though, due to the high stopping power and high linear energy transfer, the radiation dose increases greatly [12]. In case of an accidental release of these alpha emitters, a viable technique to measure the concentration of these is needed. Measuring alpha emitters directly with alpha spectrometry is very complex due to the short travel distance within media, especially if they only occur as trace part of a sample. It would require advanced, time and labour consuming chemical pre-treatment and sample preparation. Comparatively, NAA works on the basic principle of irradiating the sample with neutrons and then measuring the emission of gamma-rays when the excited nuclei decay. To be able to quantify the concentration, the activation and decay of the targeted material must be determined.

One of the main advantages of NAA is the fact that the probe does not need to be treated in any way except for the neutron irradiatio, provided the sample does fit the setup. Hence, it is a non-intrusive and non-destructive way of measuring. According to the standards set by the Consultative Committee for Amount of Substance: Metrology in Chemistry and Biology (CCQM) [13], there are only two methods which can be used as primary ratio method to determine the elemental composition of unknown substances. These two methods are Isotope Dilution Mass Spectrometry (IDMS) and NAA, and it has been proven that these two both meet the same standards [14]. As IDMS requires a complete chemical breakdown of the probe though, the use of NAA can be described as desirable when the probe is either very small or very fragile. In other cases it is mostly a question of individual dispositions or accessibility.

Previous studies [9] presented a prototype setup which shall become part of the Instrumental Neutron Activation Analysis (INAA) setup, currently under development at The Applied Nuclear Physics Laboratory at the Division of Nuclear Physics at Lund University. It consists of a Genie 16 Deuterium-Tritium (DT) neutron generator from Sodern [15], and a pneumatic transport system between its shielding cave and the detector setup. The detectors are two HPGe detectors [16] (Mirion, "GC-2018") which are oriented in a 90° angle to each other. Prior to this work, the timing restrictions imposed by sample transportation was somewhere around half-lives of 2 seconds [9]. In the INAA setup, the neutron generator will be replaced by a CANS, providing a significantly higher neutron flux; increased by factor >100, based on simulations [17]. Most parts except for the generator can then be directly transferred and implemented into the INAA setup.

1.1.1 Aims

The has three key aims which are listed as follows:

- provide measurements which can in the future be compared to simulations using FISPACTII [18]
- the setup needs upgrading to a state where measurements are automated, mostly affecting the precise operation of the pneumatic sample transport system and signalling the detectors to stop counting while the sample is not in place to measure

- specify the setup regarding timing performance and minimal detectable concentration

1.2 Background

Neutrons are so-called nucleons, meaning they build one of the two parts atomic cores (nuclei) are made of [19]. As they do not have any electric charge, they will not interact with the electrons when impacting the target samples. They will rather only interact with the nucleus itself, whether by the means of elastic scattering or absorption. The probability to interact can be described by the interaction cross-section [20]. Absorption is of primary interest here, as this changes the features of the absorbing nucleus. Gaining one neutron, the target nucleus thereby changes its isotope (as well as taking up energy from the neutron). This, in turn, in most occasions will lead to the nucleus becoming radioactive. Being radioactive means that the newly formed isotope then ideally emits some kind of measurable radiation like beta- or gamma- rays. By recording a spectrum and counting the events at characteristic energies, it is possible to quantify the target in terms of its isotopic composition.

To be able to set accelerator based NAA into context, some competing methods are going to be discussed here. As neutrons are not naturally abundant, a way to generate them is needed. They can be generated in nuclear reactions using charged particle accelerators like the cyclotron, or by taking them out of a nuclear fission reactor [15]. Nuclear reactors provide a steady and continuous flow of neutrons, however these necessitate complex and costly facilities. Recent developments are leading to the shutdown of nuclear reactors all over the world, and decreasing those resources. Therefore other means of producing neutrons are of increasing interest. One suitable way is to use a charged-particle accelerator like a Van-der-Graaf accelerator or a cyclotron to shoot particles (e.g. deuterons) at specific targets. The resulting nuclear reactions will produce neutrons of a variety of different energies depending on the specific reaction they are based on. Especially important is the DT reaction ^{3}H(d,n)^{4}He, which will also be used in the current setup. Yet another neutron source type is based on proton-induced reactions, where a target is bombarded with energetic protons, and the energy of the outgoing neutron depends on the proton energy [15]. Both of the latter two types of neutron sources will play a role within the planned INAA setup [7].

The setup which was initially presented in [9] needs to be refined significantly to be able to match the expectations for the INAA setup. Thus, substantial development work and careful gauging is needed to exploit the maximum capabilities of this setup. This will be outlined in Sec. 3.1.

1.3 Report structure

The report begins with a brief theoretical introduction into the topic given in Chapter 2. The focus of the rest of the report lies on the four main aspects of the work performed. Those are: the system development in Chapter 3, describing the steps taken to physically improve the setup. The experimental procedure is presented in Chapter 4, which is followed by the presentation of results in Chapter 5 and the discussion in Chapter 6. In the end a quick outlook into the future of this setup and potential future work is provided in Chapter 7.

2 Theory

To get a more in-depth understanding of the processes in NAA, a few important theoretical aspects will be introduced here. First and foremost the concept of the nucleus and its properties will be presented. It is a part of the atom, the individual building parts that matter consists of. More precisely the nucleus is carrying most of the atoms' mass, as well as a positive charge, opposing the atoms' electrons with their negative charge.

2.1 Nuclear phenomena

2.1.1 Nuclear structure

When looking closer at the nucleus, especially the relation between mass and charge, it becomes apparent that there are two different kinds of particles that together form it. These two kinds of particles are the protons and the neutrons (proposed by [21]). Both particles have about the same mass, but differ in their electric charge, with the proton possessing positive charge, while the neutron is charge neutral. These two particles form all observable elements on earth, with each element from the periodic table possessing a characteristic amount of protons. The number of neutrons on the other hand is not quite as strictly defined, as will be shown later.

In order for these two constituents to form nuclei, it has to be energetically favourable. This means that there is a characteristic amount of energy called binding energy giving the total amount of energy needed to fully separate the nucleons apart. This binding energy can be estimated by the semi-empirical mass formula [22]:

$$B(N,Z) = a_V A + a_S A^{2/3} + a_C \frac{Z^2}{A^{1/3}} + a_I \frac{(N-Z)^2}{A} - \delta(A) \tag{2.1}$$

where A is the number of particles in the nucleus, N is the number of neutrons and Z the number of protons. The values for the constants can be found in [22]. This formula was originally compiled by Bethe and v. Weizsäcker [23, 24].

Isotopes

We now know that each specific element has a specific number of protons and with the information that both neutron and proton possess a mass of roughly one atomic mass unit. Looking at the periodic table there are some elements which do not exhibit masses which are roughly integer multiples of this atomic mass unit. One of the reasons for this circumstance is buried in the nature of so-called isotopes, meaning atoms of the same electric charge (number of protons), that differ in the number of neutrons that are bound in the nucleus. If multiple of them occur naturally, then the mass of the atom is given as the mean value weighted by occurrence. These isotopes show similar properties when the surrounding is

interacting mostly with the electrons (e.g. chemical processes). Neutrons however are mostly interacting with the nucleus which means there can be differences in the results of NAA if choosing different isotopes of the same element for irradiation.

2.1.2 Nuclear reactions

Some isotopes of different elements can be unstable meaning they emit some type of radiation. There are three main types of this so-called radioactive decay. This can happen if the isotopes have energetically favored configurations as they show a general tendency to populate similar configurations with the lowest energy that are stable. Changes in the nucleus can also occur when the nucleus reacts with an external agent, such as an energetic particle impinging the nucleus. This is called a nuclear reaction , and the notation is standardized to give the reactant, then the incoming and outgoing particles in brackets, and then the reaction product on the right side in last. An example here could be the emission of an α particle after neutron incidence on ^{197}Au with the reaction notation being $^{197}Au(n,\alpha)^{194}Ir$.

2.1.3 Cross-sections

The cross-section is a measure for the probability of interaction between an incoming particle and a specific target. When dealing with NAA, it is specifically the cross-section of an incoming neutron with the target nucleus. This cross-section is highly dependent on the neutron energy, and characteristic for each individual isotope. Around thermal neutron energies ($\leq$25 meV) it often follows a linear decline connected to the energy ($\sim 1/v$). For higher energy neutrons (epithermal), this relation is not valid any more. Specifically, several isotopes show resonance properties in the epithermal region [25]. In order to achieve the most accurate total cross-section with a given neutron source, the product of the neutron energy spectrum and the cross-section has to be integrated according to:

$$\sigma_{tot} = \int_0^{E_{n,max}} \sigma(E) * n(E)\mathbf{d}E \tag{2.2}$$

Here σ_{tot} is the total cross-section of a specific reaction, $\sigma(E)$ is the energy dependant cross-section and $n(E)$ is the neutron energy spectrum. The integration is performed from 0 to the maximal achievable neutron energy.

2.2 Processes within NAA

2.2.1 Neutron activation

In order to determine the activation of the material within a specific sample, the relation

$$\frac{\mathbf{d}N^*}{\mathbf{d}t} = \sigma_{tot}\phi N \tag{2.3}$$

can be used. It describes the process of slowly activating the sample with a given Number of atoms N into the activated state N^*, with the total absorption cross-section from Eq. (2.2)

and the neutron flux ϕ [26].

As the activated states will always decay over time, another term is needed to describe the this property on the sample. Here it is important that compared to Eq. (2.3), it depends on N^* rather than N, slowly decaying with λ as decay-constant. This will manifest in an exponential decay function:

$$\frac{\mathbf{d}N^*}{\mathbf{d}t} = -\lambda N^* \tag{2.4}$$

The most important reaction here is $A(n,\gamma)B$, as the chosen method for analysis of the activated product is gamma spectroscopy.

Combining these two processes, gives the activity after irradiation time t with:

$$A = \sigma_{tot}\phi N\left(1 - e^{-\lambda t}\right) \tag{2.5}$$

When irradiating the sample for a sufficient amount of time, there is a point where the two processes reach an equilibrium point. There, the rate of nuclei decaying equals the rate of new radioactive nuclei being produced by activation. The maximum reachable activity of the sample A_{max} can be expressed as:

$$A_{max} = \frac{m}{M} N_A \theta \sigma_{tot} \phi, \tag{2.6}$$

where m is the mass, M is the atomic mass, N_A is Avogadro's number and θ is the abundance of the specific reaction isotope within the sample [26].

Reaching this equilibrium point is demonstrated in Fig. 2.1, where the saturation curve given by Eq. (2.5) is shown.

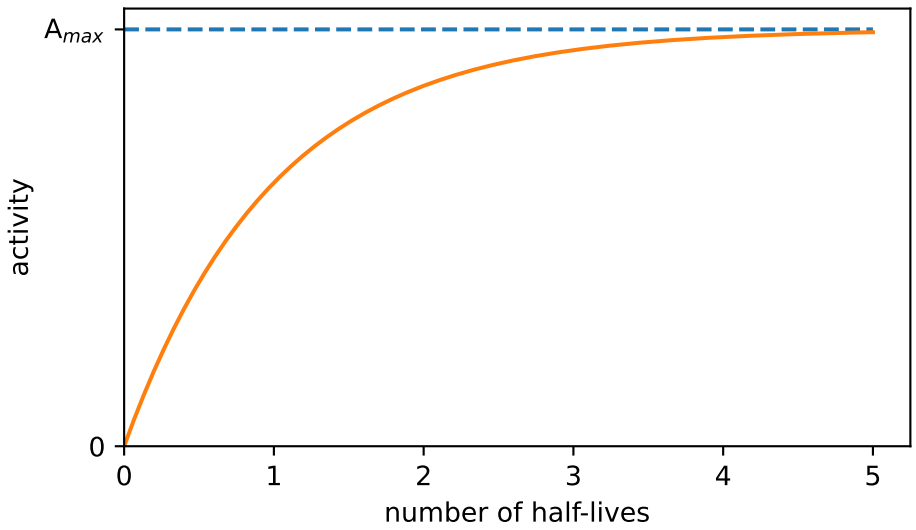

Figure 2.1: Graph demonstrating the behaviour of a saturation process common on NAA. Over the course of 5 half-lives the curve reaches a point very close to saturation.

From there on, standardized methods for performing NAA have been developed, most prominently the k_0-standardisation, first introduced in [27] and more recently updated in [28, 29].

2.2.2 Gamma ray interaction with matter

There are three main ways of interaction of gamma rays with matter that shall be quickly mentioned here. First and foremost, if a gamma photon deposits the full energy inside of the detector, it is called photopeak, with the photoelectric effect coming into play. When gamma rays travel through the detector they perpetually scatter on the electron shells in a process called Compton scattering. This might not lead to the gamma ray being fully stopped and absorbed by photoelectric effect however, leading to a continuous range of energies detected called the Compton continuum. The last effect is when gamma rays interact with the strong electromagnetic field (Coulomb field) around the nucleus creating a electron-positron pair with each 511 keV (provided that the gamma ray exceeds 1022 keV in energy). Those in turn can either be detected or not, creating so-called escape peaks at energies lower than the full-energy peak by multiples of 511 keV [30].

3 System Development

The general working principle of the setup will be described in the following section. The sample holder containing the sample is transported to the neutron generator for irradiation by the means of a pneumatic transport line. The sample is then irradiated until the activation reaches an equilibrium point, between 5 to 10 times the target decay half-life. After reaching this equilibrium, the sample is transported back to the HPGe detector setup, where two detectors record a gamma-spectrum emitted by the sample. This creates a spatial separation between the detectors and the neutron generator. The separation is crucial for the success of the system, as it reduces background generated by neutrons interacting with the detectors or the shielding material around them. A simple sketch for this principle is presented in Fig. 3.1.

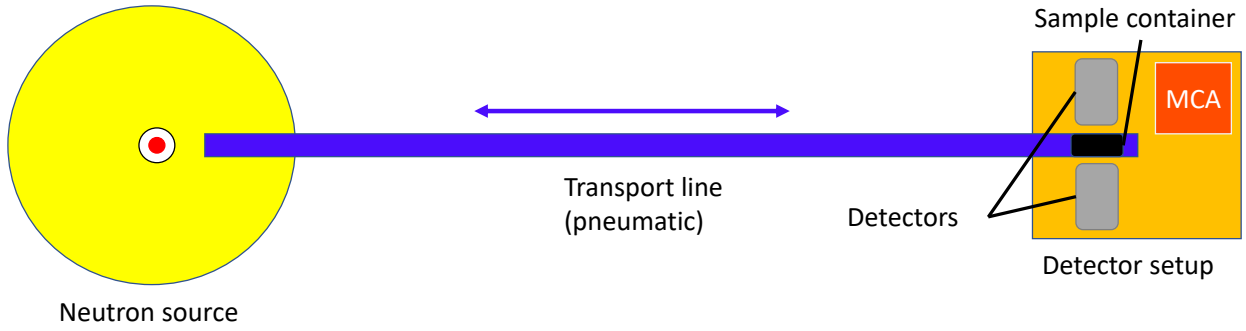

Figure 3.1: Work principle of the NAA-setup. The sample is transported between source and detectors by the pneumatic transport line.

3.1 Initial configuration and upgrade potential

In the initial configuration, the pressure was operated by four Lucifer 341B34 4-way valves. A schematic is shown in Fig. 3.2. These were controlled by a three-way manual switch connected to 24V DC. The valves were directly connected to the 7 bar pressured air system in the lab and operated in two opposing sets to send the sample-container back and forth between the detector-setup and the neutron generator. While one valve would open towards air on one side, the opposing one would open the line to the 7 bar supply. Aluminium sample holders with a mass of roughly 20 g were used, which produced considerable amounts of Compton background as Al has a relatively high cross-section (see Table A.1). As described in the outlook in [9], the largest source of uncertainties was the inability to precisely measure the times for irradiation, transport and measurement, as everything was handled manually. The average transport time was around 2 s, however there could be instances where the samples would jam in the line, massively decreasing the consistency of measurements. A sketch of the initial version can be found in [9], Figure 3.5.

For this work, the proposed improvements are listed here:

- new material and design of sample holders

- automated operation of valves and gating of DAQ system with precise time control
- increased pressure gradient

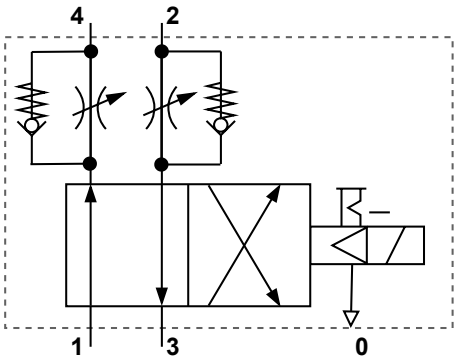

Figure 3.2: Schematic of the four valves that were used in the initial setup. Two of the valves would each form complementary sets, one opening the line on one end to surrounding air, while the other would open the line to the lab's 7 bar pressure supply line.

3.2 Implemented upgrades

3.2.1 New sample holder

To keep the Compton-scattering background from sample holders low, low-Z materials, like plastic, are the best option. The material of choice was PLA (Polylactic acid), as it is available with a 3D printer located at the Division of Nuclear Physics. The sample holder design is presented in Fig. 3.3. To determine the actual composition of the PLA, it was analysed using PIXE-analysis. Results are presented in Table 3.1. Simulations using FISPACT-II [18] performed by by R. Frost [17] showed no relevant signal is expected from the sample holders.

The sample holders have a threading of M22/1.5°(M20/1.5°) over a length of 10 mm. The sample holders have two slots on the bottom and the cap, where a screwdriver fits in, to securely screw the holder together. This prevents it from opening inside the hose by vibration. After printing, the sample holders were sanded and polished on the outside to decrease friction within the hose, and then coated in Silicone spray lubricant before each measurement was started. Over the course of the measurements some sample holders with the original design shattered. This problem was solved by a redesign with thicker walls and transitions. The maximum sample volume of the redesigned sample holder is 4.67 cm^3.

3.2.2 PLC control system

A PLC (programmable logic control) system was implemented for the pressure valve control and handling data acquisition. The system used was a Beckhoff CX9020 control unit, together with Beckhoff 24V/5V modules and programmed using TcXAEShell [33]. A sketch of the circuit diagram is shown in Fig. 3.5. Using a PLC system provided several benefits,

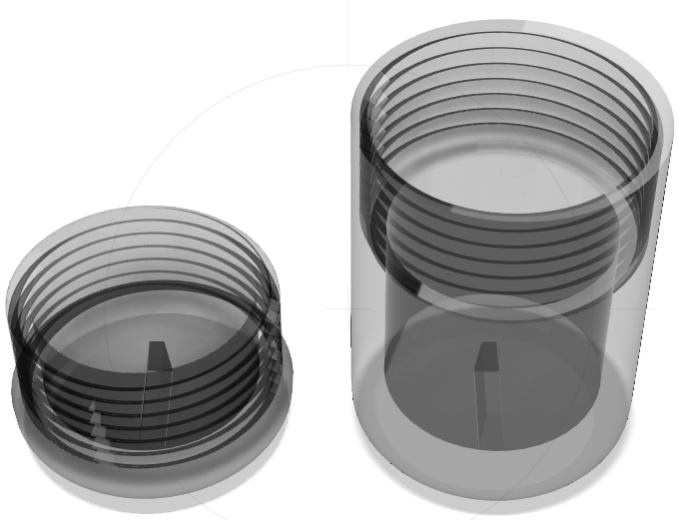

Figure 3.3: The original design of the sample holder. The inner volume is 6.616 cm^3 (later version changed to 4.67 cm^3). Edges at top and bottom are rounded to reduce the probability to get stuck in the tube. The software Fusion360 [31] was used to generate the figure.

mainly precise timing for irradiation and measurement. The final program allowed for cycling the sample back and forth with individually set times for irradiation, measurement, sample cooldown and the transport times to the generator and the detectors. This gives the cycle progression as stated in Section 3.2.3. As implemented, the cooldown time can be used to wait for the decay of longer half-life lines preventing the build-up of other lines within the sample. This is feasible, as long as they are on a similar order of magnitude (up to 10 times longer). The best example here would be a natural Hafnium sample, with one state of half-life 4 s (^{178m}Hf) and the other one with a half-life of 18.67 s (^{179m}Hf). A sample measurement cycle could then be: 1: 20 s irradiation (4*5); 2: 40 s measurement (4*10); 3: 147 s cooldown (18.7*10-40). Analysis could then take care of choosing the correct subset of the measurement in order to maximise SBR (signal-to-background ratio) as described in Section 5.1.3.

3.2.3 Pressure system

As manual driving introduces large timing errors and inconsistencies, the system was altered to work with a PLC control system. For this purpose, a complete redesign was necessary. The new system uses a set of two 5/3 way-valves (FESTO CPE14-M1BH-5/3GS-1/8) that are controlled by the PLC system. They sit on either end of the transport line, and work in an anti-parallel fashion. That means, when one side opens to the 7-bar supply pressure, the other opens to the lab, or respectively to a vacuum tank. The vacuum tank has a volume of ∼20 l and sits at the side of the detectors. With this tank it is possible to evacuate the pressure line prior to sending the sample to the detector position. Additionally, on the generator side of the line, a 7-bar pressure reserve tank was added. A diagram of the new configuration is shown in Fig. 3.6. This dramatically reduces the transport time, down to ∼300 ms in a best-case scenario. This reduction from about 2 s down to around 300 ms allows for measuring half-life ranges within a few hundred ms. The travel time towards the neutron generator does not necessary need to be as fast. This justifies opening the line only

Table 3.1: Results from the PIXE-analysis of the PLA used in the sample holders [32]. Specifically interesting are abundances of elements with a Z equal to or higher than Silicon (Z=14). The isotopes that were found, based on simulations [17], do not need to be considered in the analysis. The concentration is given with the uncertainty in parentheses.

Element symbol	**Concentration (ppm)**
Si	1145(35)
Cl	668(5)
P	359(11)
K	324(4)
S	232(7)
Ca	161(3)
Fe	29(2)
Ti	23(2)
Zn	9(1)
Cu	6(1)
Se	5(2)

towards air instead of vacuum when traveling to the generator. It still provides a transport time of 1 s, which is perfectly good for the purposes of this setup. Additionally, after each transport the over-pressure is to be evacuated to get the best overall results. The best results for the transport time back to the detectors were achieved using a venting time of 1 s and an evacuation time of 1.5 s. This gives the following general transportation cycle (reflected in the graphical user interface of the program, 3.4):

1. transport to generator (1 s)
2. vent overpressure (1 s)
3. irradiate (incl.vent time)
4. evacuate line (1.5 s, while irr.)
5. transport back to detectors ($\tilde{3}$00 ms)
6. vent overpressure (1 s)
7. measure (incl.vent time)
8. cooldown

It was found that if the overall cycle time is below 30 s, the vacuum pump faces severe difficulties keeping the target underpressure. It is strongly advised to adjust the cooldown time so the pump has time to regenerate the vacuum. This applies when studying isotopes with a half-life of 2 s and less.

Figure 3.4: Capture of the visualisation window from TcXAEShell [33]. It shows the input and control fields for the time setting for the cycles, as well as status indication lights, a button for starting the measurement and a Kill switch killing all output signals.

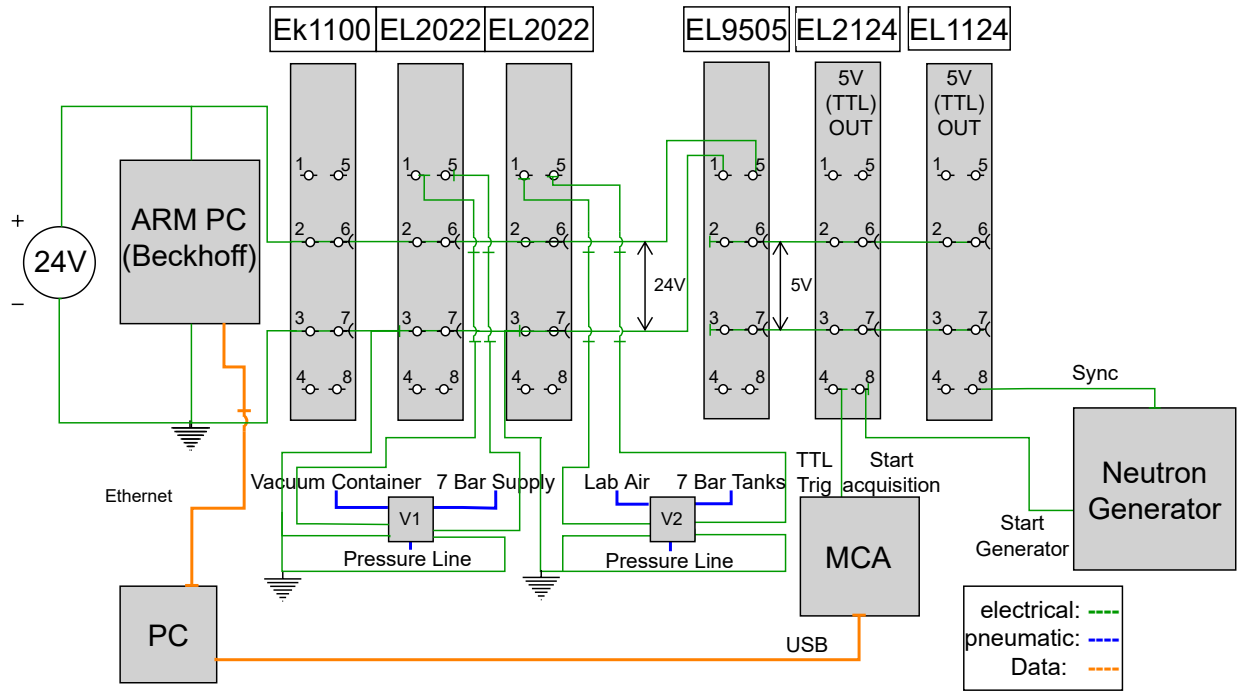

Figure 3.5: Circuit diagram for the PLC system. The Beckhoff modules control the pneumatic line valves and trigger acquisition on the MCA by gating for active acquisition. There is also the possibility to read in a control signal from the generator, as well as giving a start signal to the generator.

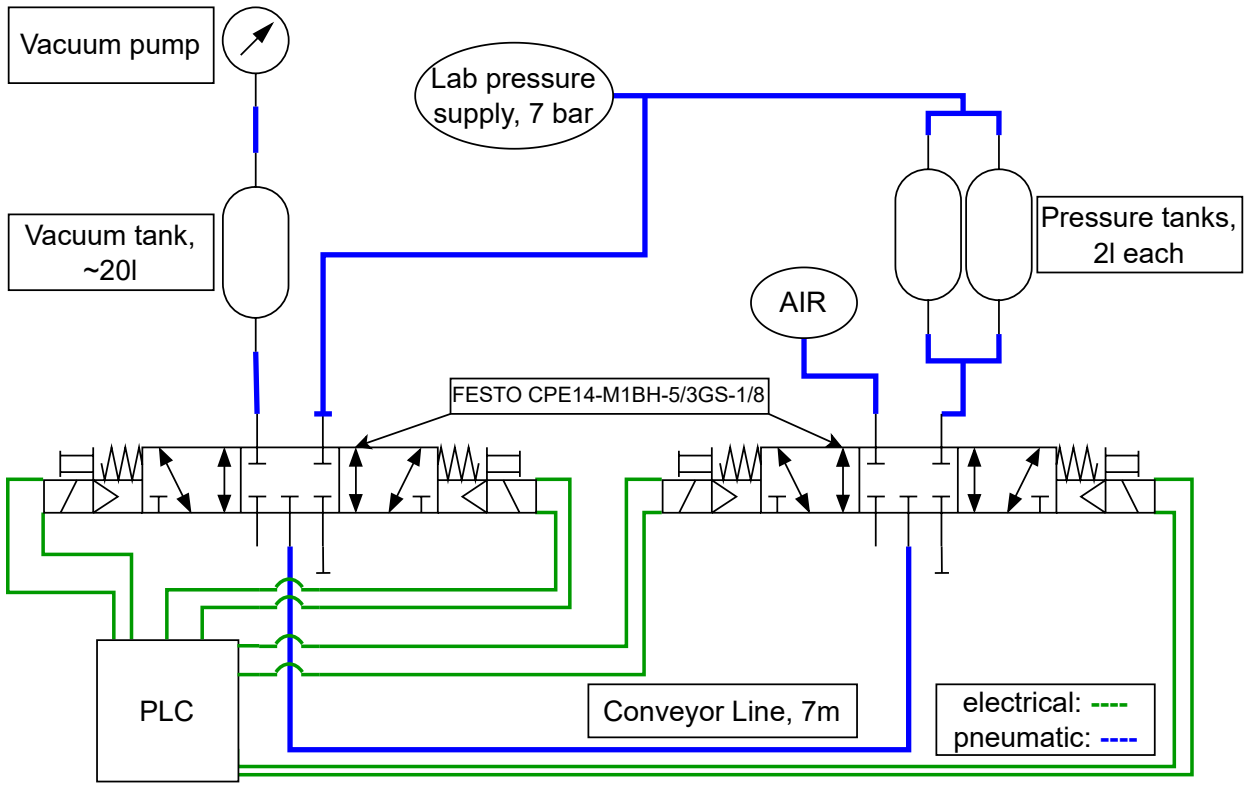

Figure 3.6: Diagram for the pneumatic system. The two 5/3-way valves are controlled by the PLC system sketched in Fig. 3.5.

3.2.4 The data acquisition system

To arrange the two HPGe detectors in a consistent manner, a detector guide was designed and 3D-printed, shown in Fig. 3.7. The HPGe detectors were connected to a CAEN DTP5780 dual channel digital MCA (multi channel analyser). It was controlled using the COMPASS software from CAEN [34]. The relevant settings were chosen following the descriptions in the quick-start guide within [35] and listed in Tables 3.2 and 3.3. The acquisition was set to record list-mode data only, reducing dead-time due to MCA memory overflow, [36]. Spectra were saved in .n42 format, whereas the lists were saved in .root format. The possibility to save the spectra in list mode is a huge benefit for the system, and offers the capability to do extensive post-processing and thus selection of specific data. The full extent of this was only realised in the late stage of the project, but provides high potential for further improved workflow and time efficiency for future measurements.

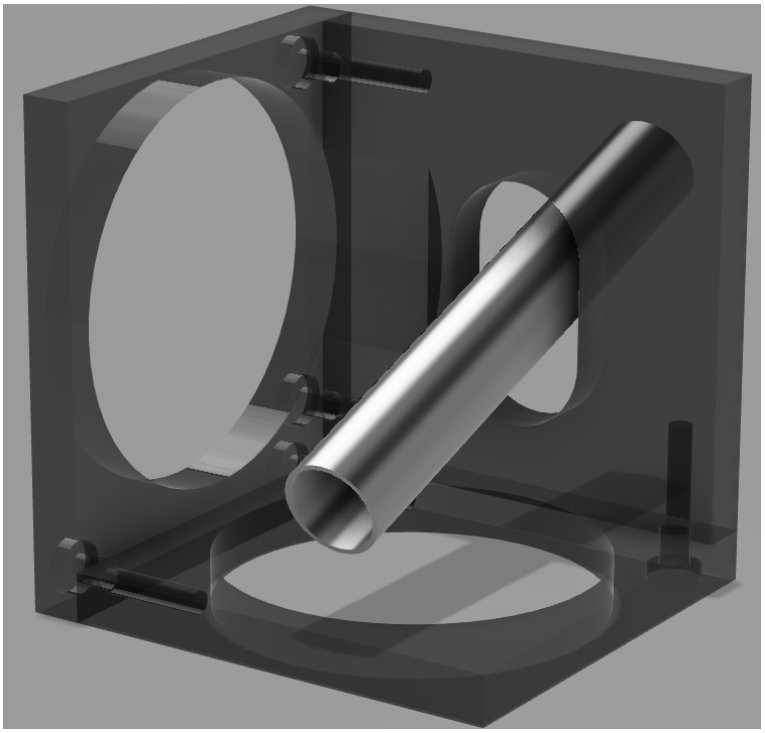

Figure 3.7: Sketch of the designed detector guide. It fixes the two end caps of the HPGe detectors and provides horizontal alignment for the steel tube containing the sample containers. Design and rendering done with Fusion360 [31].

Table 3.2: Settings within the COMPASS software configuring ADC conversion and charge integration. For the threshold, lsb stands for least significant bit.

Setting name	**Value Ch0**	**Value Ch1**
Polarity	Positive	Positive
V Set	3000 V	3500 V
I max	315 µA	315 µA
Pre-trigger	2000 ns	2000 ns
DC Offset	7.0%	0.0%
Coarse gain	7x	7x
Threshold	90 lsb	70 lsb
Trigger holdoff	800 ns	700 ns
Fast discr. smoothing	16 samples	16 samples
Input rise time	400 ns	350 ns
Trapezoid rise time	3.5 µs	3 µs
Trapezoid flat top	1 µs	1 µs
Trapezoid pole zero	40 µs	40 µs
Peaking time	75%	80%
N samples peak	16 samples	16 samples
Peak holdoff	2 µs	2 µs
Energy fine gain	1	1

Table 3.3: Settings within the COMPASS software configuring the MCA Board (DT5780, CAEN) coincidence settings. These were used to gate the acquisition with the PLC control system using a TTL signal fed into the Trig In port at the board.

Setting name	**Board**
Start mode	Software (asynchronous)
Coincidence Mode	Disabled (Background/calibration measurements)
Coincidence Mode	TRG IN level gate (NAA measurements with PLC gating)
FPIO type	TTL

4 Experimental procedures and data analysis

4.1 Measurements

The setup uses two, liquid nitrogen (LN_2) cryo-cooled, HPGe detectors (Canberra GC2018, endcap dia. 76 mm), oriented in a 90° angle to each other (see Fig. 3.7). The operating voltages are +3000 V and 3500 V.

The activation of a material follows an exponential saturation as described in Section 2.2. This means that the time it takes for the activated states to decay towards negligible levels is correlated with the amount of time it takes to activate into an equilibrium where the amount of activated nuclei equals the amount of decaying nuclei. This means that the half-life of the decaying isotope is an important property and can often be used as base time unit (then called hl) to be able to compare different isotopes.

4.1.1 Energy and efficiency calibration

In order to calibrate the two HPGe detectors, both for energy and efficiency, a set of radioactive samples were used. For energy calibration, a ^{152}Eu sample was used, as the gamma lines from this single radionuclide span a wide range of energies. From 122 keV up to 1.4 MeV there are 6 lines with a fairly equal distribution, which gives a good base to perform the linear energy calibration.

Efficiency calibration was attempted using ^{60}Co, ^{152}Eu and ^{226}Ra. However none of these sources were calibrated or provided with sufficient source strength precision, such that the efficiency calibration could be performed. Effectively, this means that while efficiency calibration is an important aspect of the setup properties, it could not be performed with the resources accessible. The method was developed for future application, but lacking the calibrated source or the use of the external-trigger-method described in [37]. Essentially it provides a test of the method, lacking absolute values, but demonstrating the expected shape of the efficiency curve.

4.1.2 Background measurement

For the background measurement list-mode data was collected with the generator running over the course of 4 h. The resulting data can then be sliced up and extracted as individual sections, matching up with all kinds of possible time configurations set within a maximum time frame of 2 h.

4.1.3 Signal-to-background-ratio

The signal-to-background-ratio (SBR) determines the detection limits of the whole system, and thus, optimising this figure-of-merit is an important step in characterising a prototype setup. To do this, the measurement procedure, mainly the irradiation and recording time, was altered focusing on one single sample which was known to give a very clear signal within the short half-life range: Indium. Natural Indium has a very high cross-section for the transition into the ^{116m2}In state that shows a high intensity line at 162 keV (see Table A.1). To double check what was stated in the beginning of this section and make sure that the full potential of the activation capabilities were used, two sets of measurements with different irradiation periods were performed. One set was irradiated for 22 s (10 periods of the ^{116m2}In half-life), the other set was irradiated for 11 s (5 periods of the ^{116m2}In half-life). This is important, as the duration of irradiation is directly affecting two things: the overall time one measurement cycle takes, and the amount of activation of other states which can contribute to the amount of background via the Compton continuum of higher-energy lines. The two sets of measurements then consisted of different recording times, ranging from 10 half-lives to 1 half-life, in order to assess the ratio between recorded counts and background accumulation. As long as the count rate from the source is higher than the background rate, this number will grow, but when the decay reaches the same rate as counts from background, it will decrease. On the other hand, the peak still has to give enough statistics in order to keep the uncertainty within reason. This means that there is an optimal point where enough counts are recorded to have good statistics overall, and the peaks still stands out against the background. A correctly performed background subtraction will impact this figure as well, pushing the SBR-value up by reducing the background within the energy range of the peak.

Table 4.1: Measurements for the SNR-study. The line that was studied in particular is the 162 keV-line from ^{116m2}In. All measurements were run for at least 30 cycles, whereas for evaluation sets with more cycles were reduced to 30 for comparability. The base time used for all the measurements was 2.2 s, the corresponding half-life of this line. The irradiation and measurement columns list the multiple of the half-life that was used (unit of half-life, [hl]). The cooldown is given either in [hl] or seconds, depending on which was applicable. The weight is given with the uncertainty in parentheses.

Sample	weight [g]	neutron flux [n/s]	irradiation [hl]	measurement [hl]	cooldown
In sample1	0.347(3)	4.7e8	5	2	14.4 s
In sample1	0.347(3)	3.5e8	5	5	20 s
In sample1	0.347(3)	4.7e8	10	2	14.4 s
In sample1	0.347(3)	3.5e8	10	5	20 s
In sample1	0.347(3)	4.7e8	10	10	20 s
In sample2	0.286(5)	4.7e8	5	1	9
In sample2	0.286(5)	4.7e8	5	3	7
In sample2	0.286(5)	4.7e8	5	4	6
In sample2	0.286(5)	4.7e8	10	1	9
In sample2	0.286(5)	4.7e8	10	3	7
In sample2	0.286(5)	4.7e8	10	4	6

4.1.4 Sample measurements

Logging the data as lists allows for maximal freedom in post-processing, including dead-time estimation, proper background-subtraction and time-slicing of the measurement data. Additionally it provides the capability to perform decay-analysis and coincidence measurements.

To find an efficient way of measuring, the general rule set was when measuring a sample the maximal measurement time was 2 h. In order to reach a statistical uncertainty of 1% the amount of counts within one peak (without background) needs to be 10000. This is considered enough precision to stop the measurement in case any particular sample reaches this threshold before reaching the 2h-threshold. This constraint will of course decrease yield as soon as the isotopes of interest have half-lives on the order of minutes or longer (giving full cycle durations of 15-20 minutes and thus only single-digit number of cycles). But as this work will focus on short half-lives (under one minute), this seemed a valid choice to base a standardized measurement procedure on. Specifically, for the steel sample PIXE analysis was also performed by [32] in order to determine the composition and match it against the results observed. Results are presented in Table 4.3.

Table 4.2: Details of samples measured. The table lists the sample composition as well as the half-life of interest (listed as base time). This gives the base time for the factors for irradiation and measurement times. The cooldown is given either as multiple of the half-life (without units), or as the time in seconds, as for very short half-lives the cooldown was stretched out for the sake of the vacuum system to recuperate.

Sample	Composure	weight [g]	base time (s)	irradiation/ measurement	cooldown	cycles
Pure samples						
Ge	metal	6.874[3]	0.5	10/10	15 s	180
Gd	Gd_2O_3	2.000[3]	220	10/1	9	4
Au	metal	0.201[6]	7.73	10/1	9	20
In sample1	metal	0.347[3]	2.2	see Table 4.1		30
In sample2	metal	0.286[5]	2.2	see Table 4.1		30
Hf	HfO_2	1.300[4]	4.0	10/5	5	30
			18.67	10/1	9	10
mixed samples						
NaCl	Salt	2.846[4]	0.715	10/1	22 s	120
Steel	see Table 4.3	19.346[6]	210	5/1	0	6
Soil sample1	unknown	2.484[2]	-	1/1	-	1
Soil sample2	unknown	2.949[9]	4h	1/3	-	1

4.2 Data analysis

The data analysis was performed using python, and specifically the PyROOT package [38], especially since this allowed for efficient data storage using the .root file format for the storage intensive list-mode files. Throughout the next chapters, data from the two detectors will be labeled as Channel 0 or Channel 1 referring to detector 1 and detector 2 respectively.

Table 4.3: Results from the PIXE-analysis of the steel bolt. Comparing with Table A.1 and the results in Fig. 5.5c, the interesting reactions within the sample are mostly ^{56}Fe(n,γ)^{56}Mn, ^{55}Mn(n,γ)^{56}Mn, and ^{27}Al(n,γ)^{28}Al. Results provided by [32].

Element symbol	**Concentration (‰)**
Fe	585.5(2.0)
Cr	181.1(1.6)
Ni	111.8(1.5)
Al	79(24)
Nb	23(1.9)
Mn	6.3(0.3)
Co	5.7(0.6)
Ti	4.2(0.1)
Cu	1.6(0.1)
Ca	0.8(0.1)

4.2.1 Energy and efficiency calibration

Generally, energy calibration was performed using an ^{152}Eu-source, the Compton-subtraction method from ROOT and fitting the peaks assigned by intensity. The centroids were used to find the energy calibration via a linear relation between bins and energy. An example plot of the fitted peaks within the Eu-spectrum is shown in Fig. 4.1.

For general detector efficiency calibration ^{152}Eu and ^{226}Ra were used. The efficiency fit function for the HPGe detectors was [39]:

$$\ln \varepsilon = \{(A + Bx + Cx)^{-G} + (D + Ey + Fy)^{-G}\}^{-1/G} \tag{4.1}$$

where $x = \ln E_\gamma/100$ and $y = \ln E_\gamma/1000$. ε is the efficiency and all other factors (A...G) are constants. The different spectra were normalized to the intensity of ^{60}Co at 1332 keV. The overall plot is shown in Fig. 4.2. It has to be noted that the efficiency units are more or less arbitrary, in a way explained with the figure as well as in the discussion.

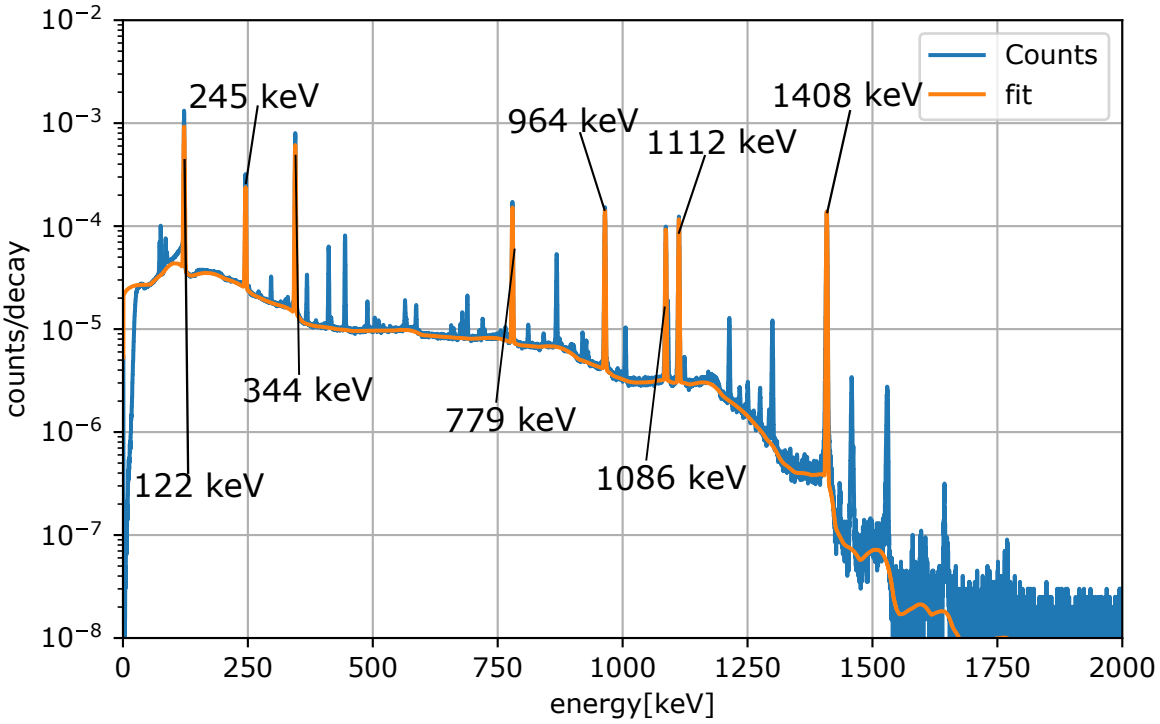

Figure 4.1: Gamma-ray spectrum for the ^{152}Eu-source used for energy calibration. The plot shows the fits for the lines which are above 5% relative intensity. The energy calibration consists of a linear fit of the corresponding energy to the 16384 bins within the recorded spectrum.

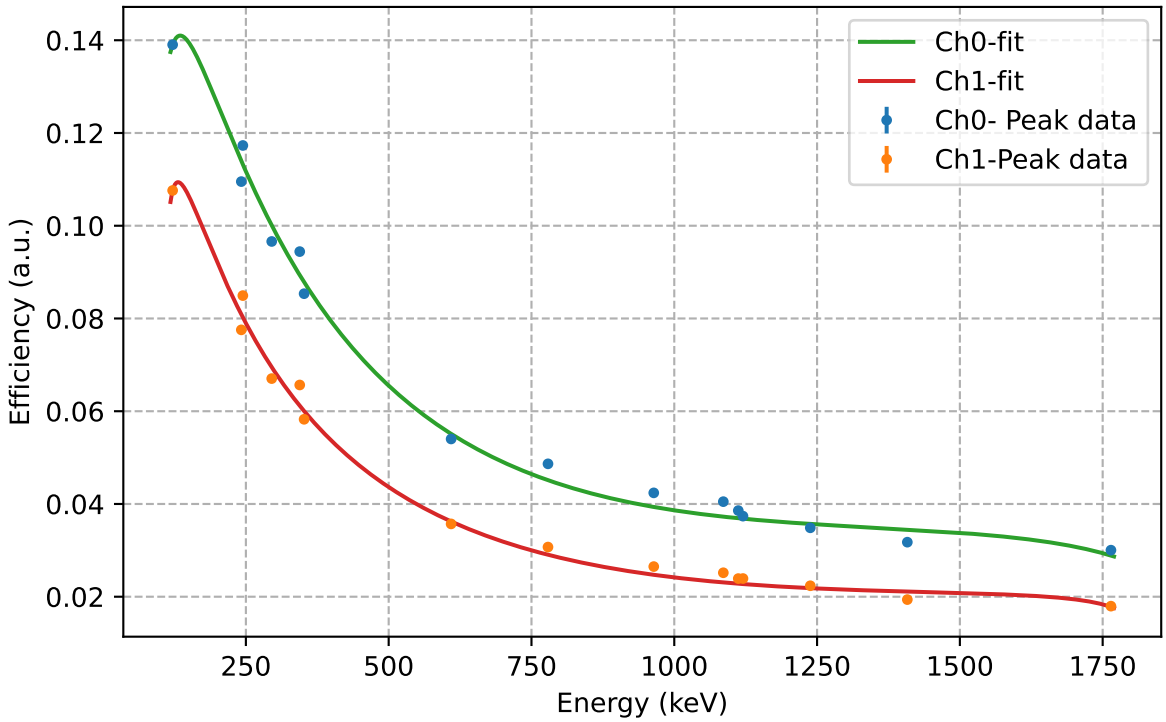

Figure 4.2: Efficiency curve of the two detectors. The data combines ^{152}Eu and ^{226}Ra data combined by normalising to the efficiency for ^{60}Co at 1332 keV. The fit is performed using Eq. (4.1). It is important to note that this is not viable as absolute efficiency measure, due to the uncertainty in the source activities. Uncertainties plotted are based only on Poisson-statistics of the counts within the fitted peaks. Using a calibrated source or the external-trigger method ([37]) would be able to provide this though. According to the manufacturer, the relative efficiency of these detectors is ∼20%, and although the measurements here are not taken at 25 cm distance, it still seems like the estimation could be a little bit too high here. This should be fixed using either of the proposed methods.

4.2.2 Dead-time estimation

When using COMPASS and the DT7580, according to [35] the on-board dead-time (Θ) estimation is performed:

$$\Theta = 1 - \left(\frac{OCR + \text{saturation events}}{ICR_{CAEN}} \right) \tag{4.2}$$

where OCR is the number of true counts, and ICR_{CAEN} is the sum of all registered events, plus pile-up events (such counted twice), and counts missed within the dead-times, interpolated by Monte-Carlo (MC) simulations. However, when using the gated acquisition mode, according to CAEN [36] the implemented dead-time estimation would not be correct. Thus, the dead-time estimation had to be performed using the list-mode data according to:

$$\Theta = 1 - \left(\frac{OCR}{ICR_{own}} \right) \tag{4.3}$$

starting with the simplest case, ICR, and step by step increasing the complexity to better match up with the one in Eq. (4.2). Here ICR_{own} =total events + pile-up events and OCR is the same as before.

Tested on a data-set taken in un-gated acquisition mode and compared with the estimated live-time data from COMPASS, this method provided unsatisfying results. For further refinement, in accordance with the manufacturers advice [36], the saturation decay time was taken into account as described in the MCA manual [40]. The procedure there is to use the trigger that signals saturation, get the time difference between it and the next trigger, which signals a new correctly taken trigger, and declare everything in between as dead-time. With this, the result of this study is presented in Fig. 4.3, showing two regions plotting the dead-time calculated using this method against the dead-time calculated by COMPASS. The dead-time calculation shows a linear correlation, however the estimation is slightly higher for the manual determination.

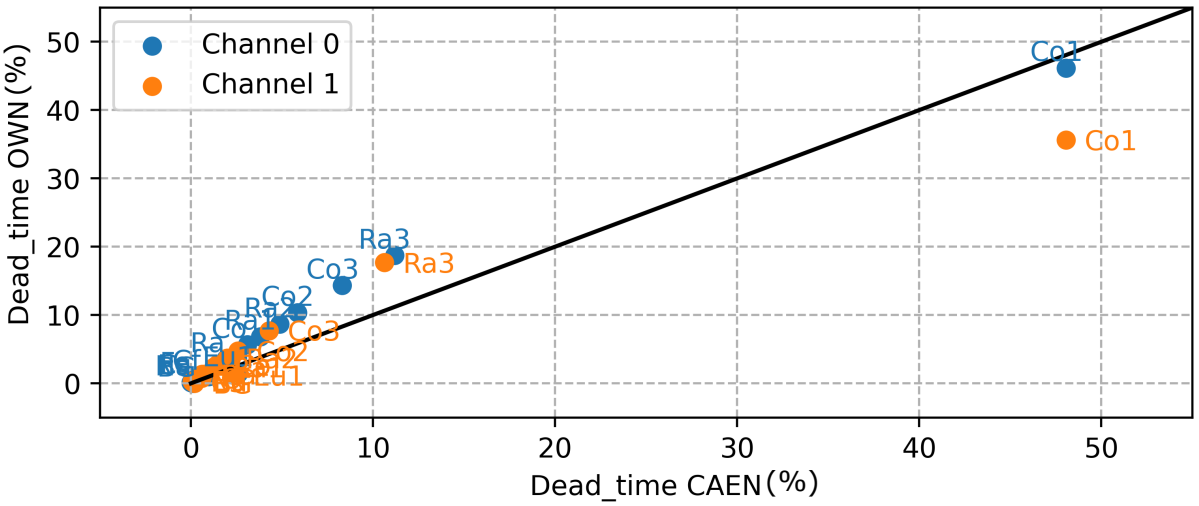

(a)

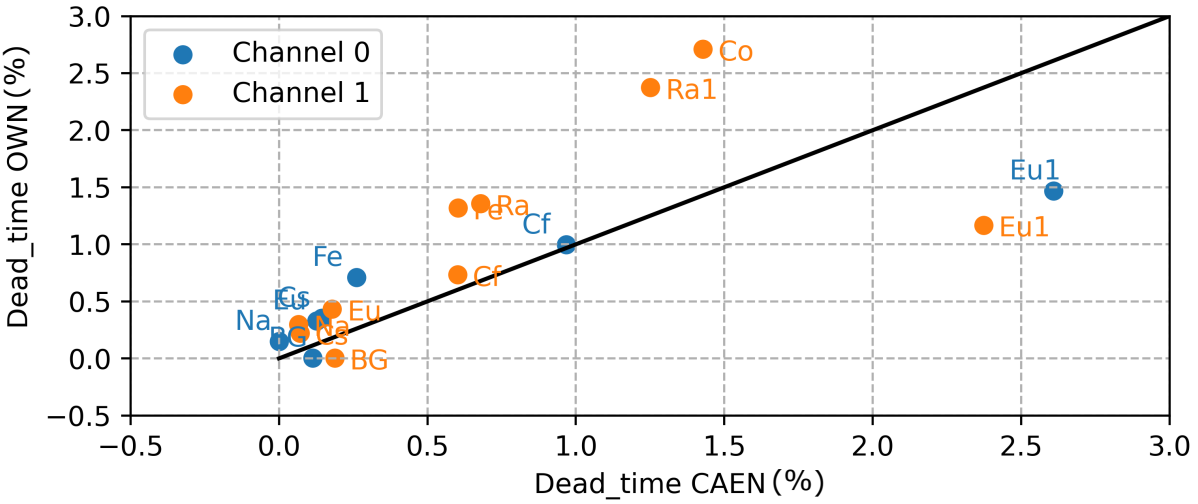

(b)

Figure 4.3: Demonstration of the deadtime estimation produced by the programmed algorithm (OWN), against the intrinsic dead-time estimation performed by COMPASS itself. Here a) shows the full range, while b) is zoomed in to the lower end of the data. The black line indicates the line of equality. The relation seems to be linear, except for the two measurements that show up underneath the equality line. This is discussed in Section 6.1.2. For this purpose a wide range of sources was used, some with different distances between detector and source (indicated by numbering) in order to get a wider range of dead-times. The isotopes used were ^{24}Na, ^{55}Fe, ^{60}Co, ^{152}Eu, ^{226}Ra and ^{252}Cf, plus one measurement without any source (BG).

4.2.3 Noise level analysis

In order to determine the noise level of the detectors, the background measurement was sliced up into 30 second long dead-time corrected slices, and then grouped into odd and even sections. These two histograms were then subtracted from each other, to give a noise level estimation. The mean should be close to 0. For the noise curve, that will depend on the amount of counts in the background at the different energies. Therefore an exponential was fitted.

4.2.4 Background correction

In order to perform the best possible background subtraction, which fits all different kinds of data-sets, a continuous spectrum was recorded for the duration of 4 h of running the generator and consecutive 12 h of cooldown in list-mode acquisition. To match this up with the different spectra, as all the timing information is there, slices of the background data can be extracted to exactly match up with the acquisition measurements. The slices are the intervals in which measurements were taken, interrupted by the periods for cooldown, irradiation and transport. Of course, for correct subtraction, these slices have to be properly background-subtracted, which means calculating the dead-time for each slice individually in order to account for longer-lived activation products. One relatively simple way of doing this is to just add the dead-time in time-format and then reconvert into percentage in the end. After selecting this background data, it was converted into histogram format and subsequently subtracted from the sample data histogram, accommodating for the difference in dead-time. As an example for the application of this method, two versions of the SBR-study were executed, one with background subtraction, the other one without. It has to be noted here, that the background data had to be adjusted by a multiplication factor, due to changes within the surrounding lab environment, which also affected the two detectors differently due to geometry. The conversion factors were applied as rate corrections, giving a factor of (3.1e8/4.7e8) for channel 0 (detector 1) and (3.1e8/4.7e8) for channel 1 (detector 2).

4.2.5 Signal-to-background-ratio

The data for the SBR-study was dead-time corrected, and then the peak at 162 keV was fitted within all spectra using a gaussian fit inside a defined boundary on top of a linear background fitted outside of the boundary. As the initial sample had to be replaced, a correction for the weight of the second, lighter sample had to be made as well.

The dataset was analysed twice in two different versions, one without any background subtraction, and the other one with subtraction. Notably, as the subtracted spectrum should yield a "clean" spectrum, it provides the opportunity of more appropriately correcting for the sample weight, as this method is able to account for the Compton background to be scaled. This is not possible in the non-subtracted version, as it is not possible to distinguish between normal background and Compton background. Section 6.1.5 will go into more detail regarding this circumstance.

4.2.6 Decay analysis

Identifying a peak within a gamma-spectrum and linking it to an isotope and line can often be challenging, as there are usually several isotopes with lines that have similar energies. As long as their lines are not clearly outside of the resolution restrictions of the detector system, it is not immediately clear what is actually detected. In order to further investigate specific lines, this setup allows to further narrow down the possible candidates by investigating the half-life of the recorded line. For the purpose of analysing a single line in more detail, the rate of counts within the region of that specific line can be evaluated over the course of multiple cycles. Therefore the list-mode data is sliced up into the different cycles by the means of finding large time gaps between two neighbouring list entries. Once this is done, a time window is chosen wherein the counts will be integrated. Within the time window, all counts inside of a selected energy window are added up. That data is then corrected for background by subtracting the mean between the two adjacent same-size energy windows on each side. This should account for both the general background and the Compton-background from higher lines. As these are already subtracted, the fit-function f(t) is expected to only be a regular exponential decay without offset like:

$$f(t) = A * e^{-0.693 * t / T_{1/2}} \tag{4.4}$$

where A relates to the initial activity and $T_{1/2}$ is the half-life of the decay. t here is the time after irradiation.

4.2.7 Coincidence analysis

To analyse coincident events within the two detectors, a so-called coincidence matrix needs to be built. With the list-mode data this can be performed by setting a specific time window within which the coincidence has to take place. This coincidence window depends on the specific state transitions happening in coincidence. If one of the states is meta-stable, the coincidence window needs to be much longer than if the deexcitations are allowed transitions and the product of the decay process reaches the ground state within nanoseconds. This coincidence matrix can then be displayed in a 2D-representation (see Section 5.2.3).

For the coincidence analysis a spectrum from a ^{60}Co-source was analysed. The data from the two channels was read in, dead-time corrected and calibrated. Subsequently, the coincidence matrix was generated using a coincidence-window of 500 ns. With ^{60}Co, the two interesting peaks in coincidence have energies of 1173 keV and 1332 keV. Thus, the chosen window for plotting was between 1100 and 1400 keV. For the purpose of getting more detail, the matrix projections onto one dimension is included as well.

5 Results

In this section the results of the measurements are presented. The section is grouped into the results of the measurements that were mainly targeted towards testing the setup and finding the best measurement procedure, and the measurements that should show what the setup can do in terms of actually measuring some samples and analysing a few different samples.

5.1 Determination of setup parameters

In order to determine the best measurement procedure, a set of measurements were taken, using the Indium sample with its strong peak at 162 keV. It shows a very prominent peak against background in all configurations, which means it will serve very well in gauging the optimal measurement procedure.

5.1.1 Background determination

A background spectrum was collected for 16 hours after the generator had reached a stable neutron output of 4.7e8 n/s. In Fig. 5.1, 30 min slices from that spectrum are displayed, showing the last 30 min of the generator running, and the 2 consecutive slices thereafter. It's very apparent that the rate drops dramatically as soon as the generator is shut off. It has to be noted here, that there were some changes to the general lab environment in the lab before the background measurement was taken, due to the rearrangement of another experiment. Most notably, a large amount of lead was removed from the vicinity of the detectors and close to the generator. As lead provides one of the most apparent contributions to the background (either from prompt or delayed gamma emission from neutron activation), this means that there are some issues with the background subtraction which will be discussed in Sec. 6.1.4.

5.1.2 Noise level determination

For the noise level determination, the part of the background measurement where the generator was running was used. As stated above, the resulting two lists (odd/even slices) were compiled into spectra and then subtracted from each other. The difference provides a measure for the noise that is to be expected from the detector. The results suggest that the noise level is not constant over the range of the spectra (see Fig. 5.2), which is why an exponential function was fitted to the data. For this purpose the data was binned by a factor of 128 and then the absolute value of the counts was multiplied by a factor of 3 to serve as upper boundary for expected noise (giving a worst-case estimation). The equation used for fitting is:

$$\mu(E) = Ae^{-bE} + c \tag{5.1}$$

where E is the energy, μ is the noise, and A, b, c are constants. The fit coefficients for the two detectors are given in Tab. 5.1.

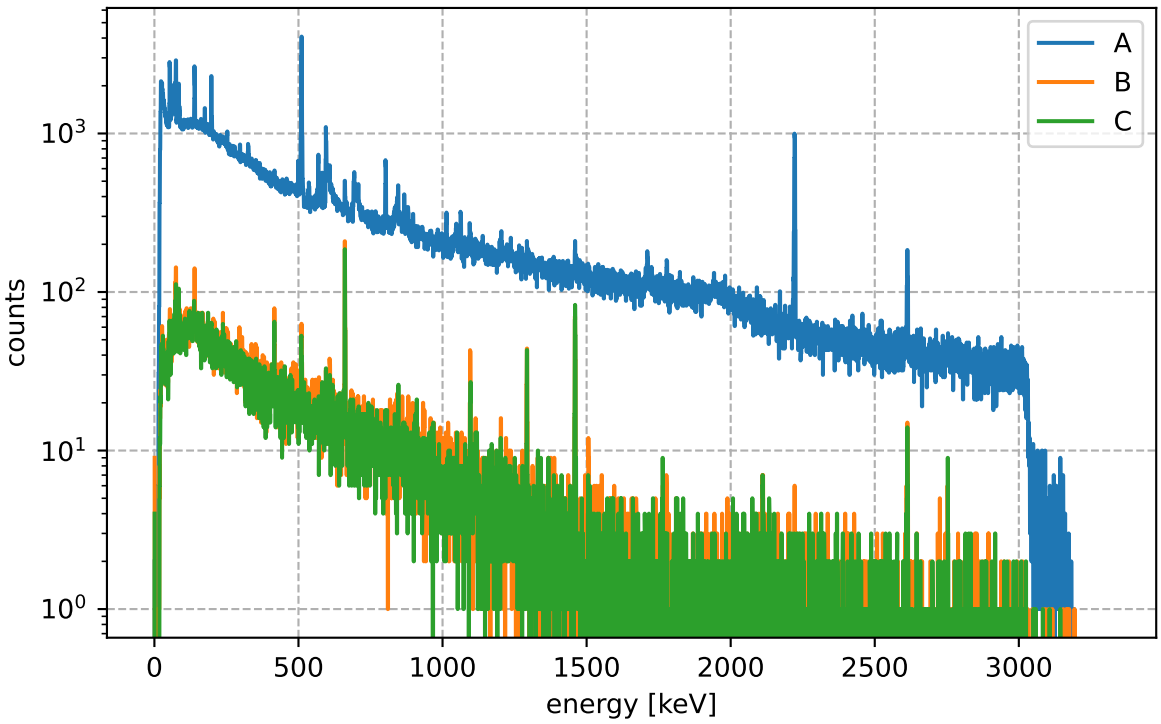

Figure 5.1: Three spectra from the background measurement, all taken from a 30 min time slice. Spectrum A is taken while the generator is still running, the other two are the two 30 min slices thereafter.

Table 5.1: Fit coefficients of the exponential function for the noise within the two channels.

A	b	c
8.68 ± 0.02	$1.12e-03 \pm 4e-09$	$0.45 \pm 0.03e$
8.60 ± 0.03	$1.07e-03 \pm 3e-09$	$0.03 \pm 0.02e$

5.1.3 Signal-to-background ratio study

When trying to fit a gaussian on top of the background to get the SBR, the method propagating all errors produced significant uncertainties. A better version was found by summing the counts in the background (determined by fit) and the peak and using the statistical uncertainty for both respectively. This is done in an effort to optimise for signal strength and minimise the overall measuring time, in order to get the best SBR within the least amount of time. Studying the three different plots in Fig. 5.3 a few things can be concluded: First, the counts within the background seem to follow a linear trend, which is to be expected for constant levels of background radiation. Secondly, the counts within the fitted peaks (Fig. 5.3b) seem to converge against a maximum value, which complies to the properties of

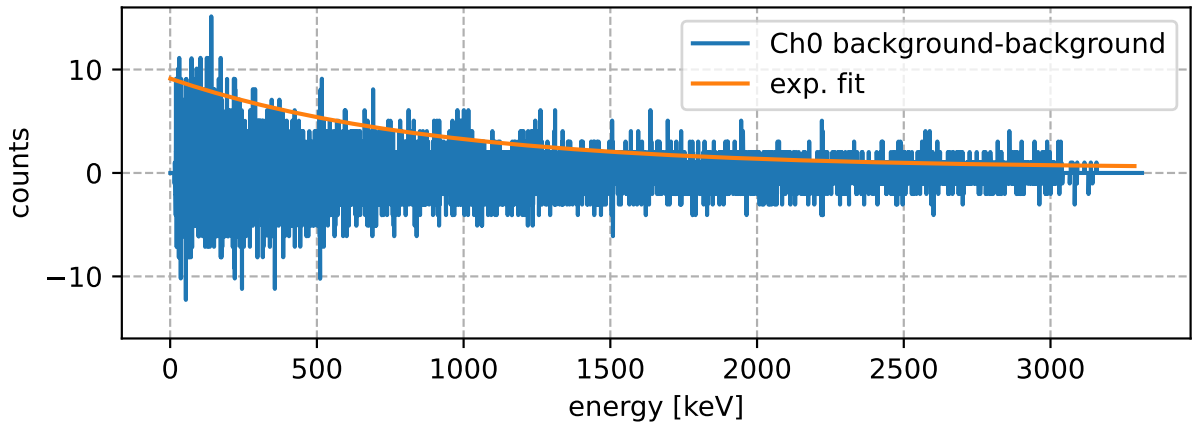

(a) Noise and fit function for Channel 0

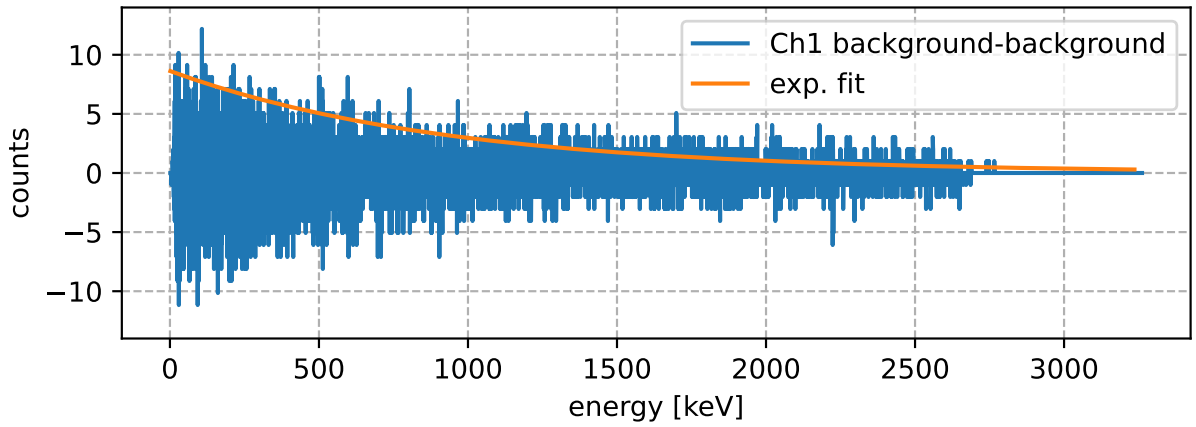

(b) Noise and fit function for Channel 1

Figure 5.2: Plot of the determined noise (the difference between the two different summations of the background spectra, in 30 s alternates) and the exponential fit to the data retrieved by fitting an exponential decay to the absolute value multiplied by a factor of 3 after rebinning the data by a factor of 128. The fit results are listed in Tab. 5.1.

the integral over an exponential decay. Lastly, Fig. 5.3a shows that while not performing background-subtraction, measuring for only one half-life will provide the best SBR and thus, should be the base for evaluating spectra. The relation this curve should follow is the ratio between the integration of the decay counts against the linear background which can be expressed by:

$$SBR = \frac{\text{Signal}}{\text{Background}} = \frac{A(1 - e^{-bx})}{Cx} \tag{5.2}$$

where A is the total number of counts in the integrated spectrum for the maximum measurement time, b is the decay constant of the lines exponential decay defined as $b = \frac{\ln 2}{t_{1/2}}$ and Cx is the linear function of the background that cannot have any offset.

When subtracting the generator background, the general shape of data within the three plots in Fig. 5.4 still stays the same, which can be explained by understanding the background counts underneath the peaks as Compton background from higher lines (like for example

the 1097.33 and 1293.56 keV lines from ^{116m1}In with a half-life of 14.1 seconds), whereon the peak is situated.

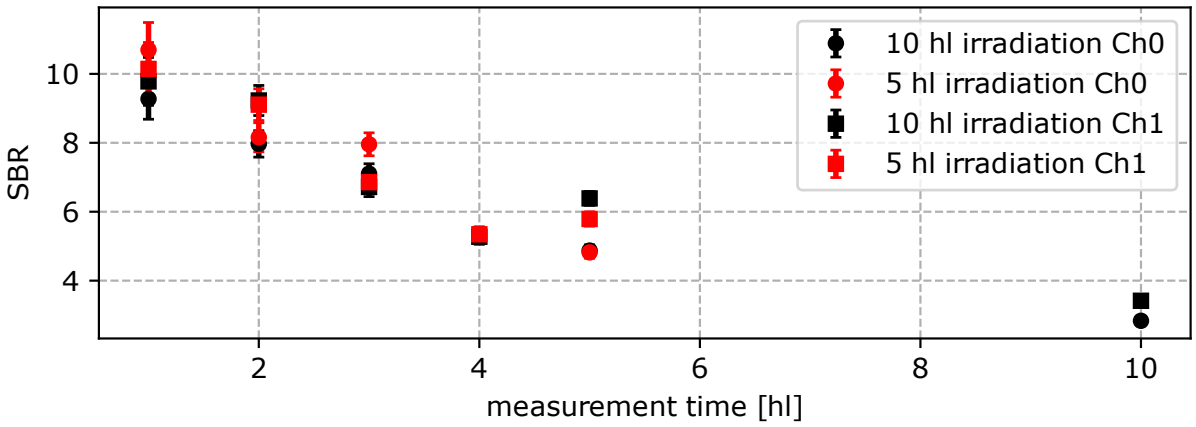

(a) Signal-to-background ratio without generator background subtraction.

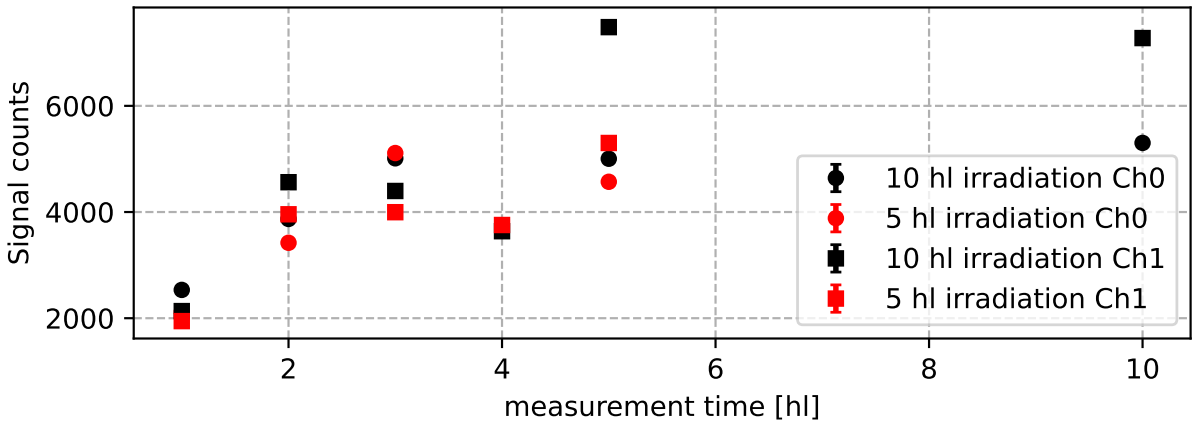

(b) Signal accumulated for the different points in the SBR-study.

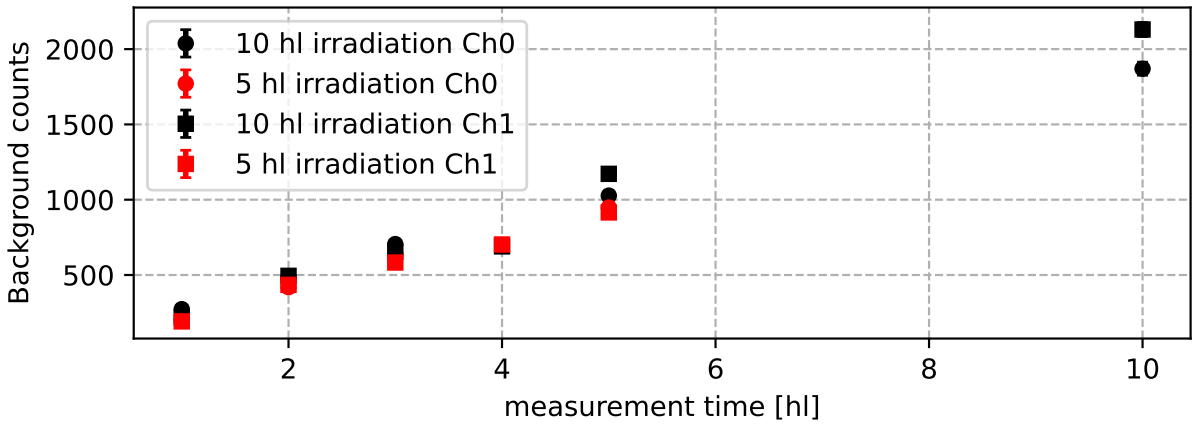

(c) Fitted overall background without subtraction.

Figure 5.3: Results of the SBR-study. For this, the Indium sample was run with different time sets: Both for 10 and 5 half-lives measurements were taken with measurement intervals being multiples of the 162 keV line half-life of 2.2 s. After measuring the samples were set to cool down at the detector end until the sum of measurement and cooldown time reached the sum of 10 half-lives (i.e. 22 s), reaching a negligible level of activity of this line. While the signal in b) seems to follow a saturation, at least the lower end in a) indicate a fairly linear relation most likely due to the linear background. The point with the best SBR is thus reached when measuring for only one half-life.

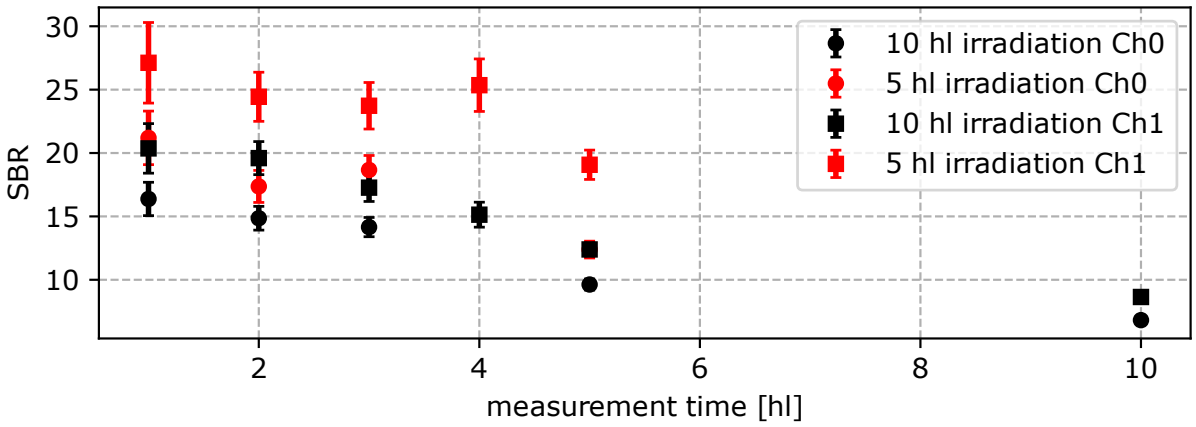

(a) Signal-to-background ratio with generator background subtraction. The points indicate a linear relation with the optimal SBR reached with only one half-life of measurement as well. The overall magnitude for the SBR is higher compared to Fig. 5.3a.

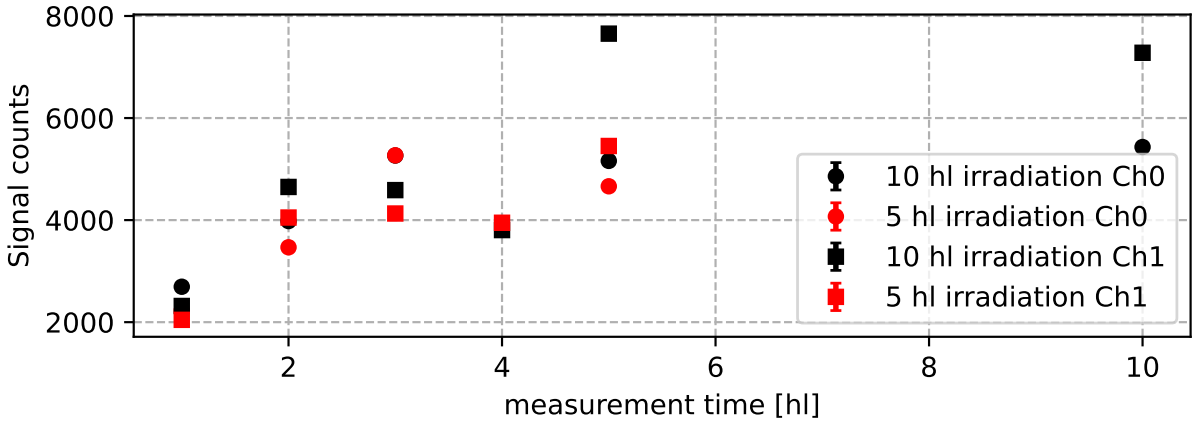

(b) Signal accumulated for the different points in the generator background subtracted SBR-study. The data seems to be very much similar to Fig. 5.3b, indicating that the change in SBR is mainly caused by reduced background.

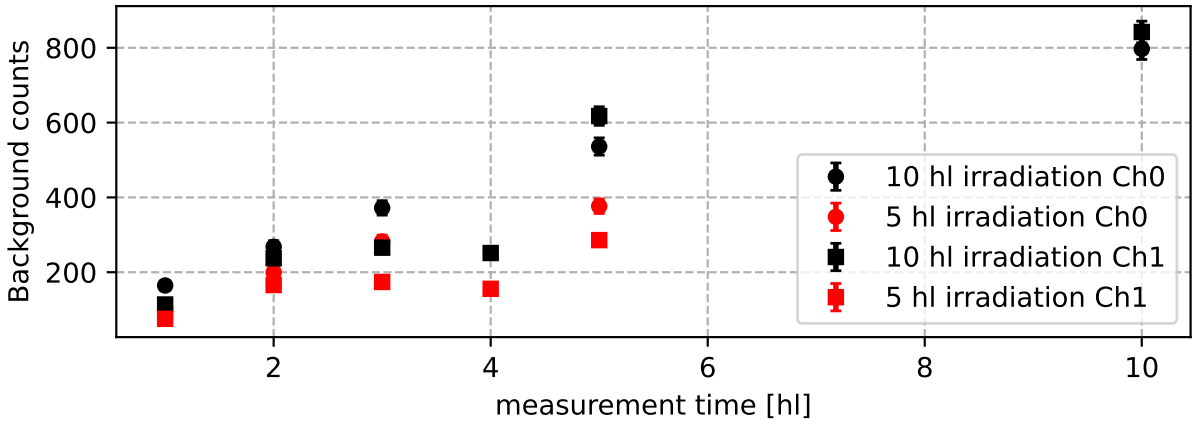

(c) Plot of the fitted Compton background with subtracted generator background. The background still shows a fairly linear increase, though it is not as clear as in Fig. 5.3c.

Figure 5.4: The same three figures as presented in Fig. 5.3, only that now generator background subtraction was performed on this set. There is a clear difference in the amount of background counts, here only originating in the Compton continuum part of the higher-energy lines.

5.2 Different measurement types

5.2.1 Spectral analysis

The analysis of the spectra was performed by first generating dead-time corrected spectra, and then subtracting the corresponding generated background spectrum. This cleaned-up spectrum was then searched for peaks, and matched with the lines which correspond to the individual isotope. A few sample spectra are displayed in Fig. 5.5, while the full list of fit parameters and peaks found for the individual channels of all samples listed in Tab. 4.2 is presented in Table B.1 (in the Appendices).

Table 5.2 shows the detection limits for a few single elements. These were determined by calculating the mass corrected for sample constitution and then normalising the fitted peak to the noise level in the respective detector channel. This should give a lower bound on the minimal amount necessary in order to still see the peak against the noise from the detectors. The detection limits for the listed isotopes are on the order of mg. In order to determine this limit Eq. (5.3) was used, where m is the sample mass, μ is the noise from the respective detector determined in Sec. 5.1.2 and A is the number of counts within the respective characteristic peak determined by fit.

$$lim = m_{element} * \mu_{ch}(E)/A \tag{5.3}$$

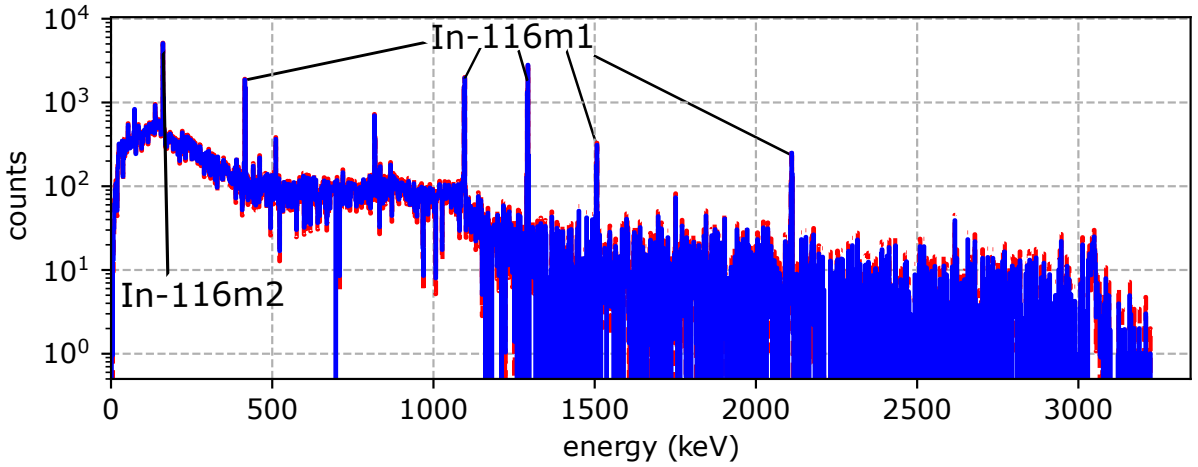

(a) Gamma spectrum of the neutron-irradiated In sample from the 10 hl irradiation/10 hl measurement run. The spectrum shows the 2.18 s half-life line at 162 keV from ^{116m2}In, and 5 peaks from the other metastable state (^{116m1}In) with a half-life of 14.1 s.

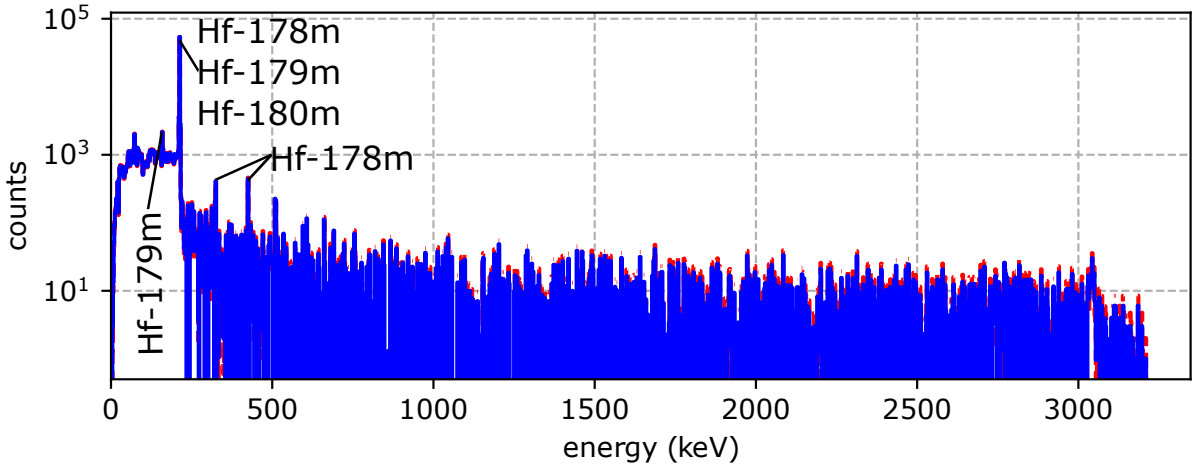

(b) Gamma spectrum of the neutron-irradiated HfO_2 sample. The peak at 214 keV shows up very strong with three different reactions contributing each with different half-lives. The other three lines from Hf are only from one isotope.

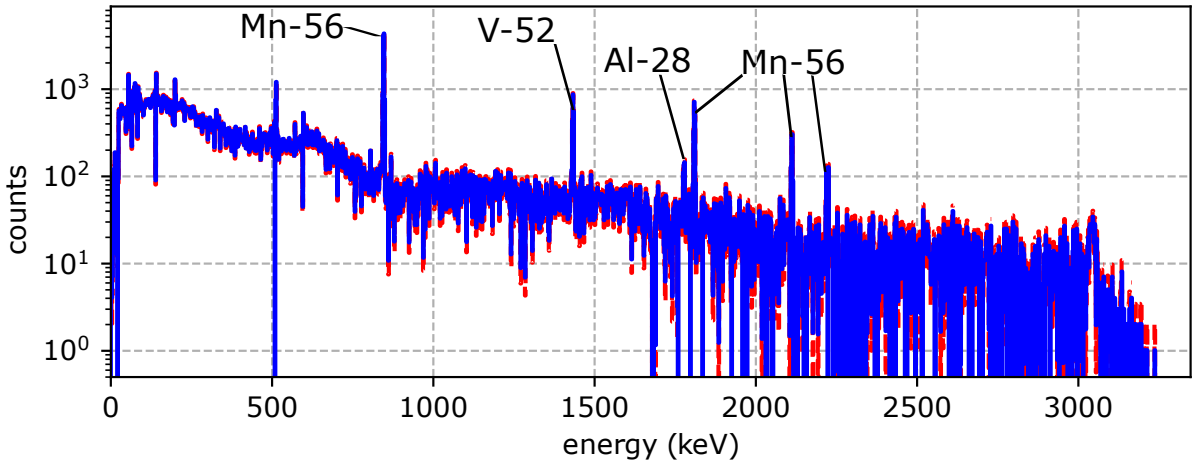

(c) Gamma spectrum of the neutron-irradiated steel bolt. The most prominent activation product here in ^{56}Mn, which is most likely either from the activation of ^{56}Fe, or from the small amount of ^{55}Mn that is present in the steel sample (see Table 4.3). This is indicated by the presence of the ^{52}V-line which is an activation product of ^{55}Mn, but not of ^{56}Fe.

Figure 5.5: Three exemplary Background subtracted gamma spectra for In, Hf and Steel. The peaks that could be associated to lines from the different isotopes produced in the NAA are labeled, more information on the fit to the peaks can be found in Table B.1. The spectra are all taken from Detector 1.

Table 5.2: Detection limits for the different elements. The values were determined by assuming a linear correlation between sample mass and signal strength, and then scaling the peak towards the noise level, to find the point where the it will stand out against background (see Eq. (5.3)). The masses were corrected by percentage of weight within the compounds. This means the detection limit gives the minimal total mass of the element (within a sample) needed for detection.

Element	Weight[g]	Detector	fitted Energy [keV]	max peak size	Noise level	Detection limit
Indium	0.347	2	162.88	7225	7.26	0.35 mg
Hf (HfO_2)	1.102	2	214.67	63040	6.87	0.12 mg
Gd (Gd_2O_3)	1.738	1	360.76	444	6.25	24.5 mg
Gold	0.201	1	279.5	136	6.80	10 mg
Na (NaCl)	1.118	1	1634.07	532	6.80	3.9 mg

5.2.2 Decay study

To show the capabilities of the setup in regards of analyzing a singular line in even more detail, like for example validating the assignment towards the correct isotope via its half-life, the 162 keV line of ^{116m2}In was analyzed in Fig. 5.6. The data was taken from within an energy window of 162 ± 2 keV. The fit to Eq. (4.4) yielded a result of $\beta = 2.012 \pm 0.0025$ s for the half-life and $A = 257 \pm 16$ counts for the activation factor. The actual half-life of 2.18 seconds is not within the uncertainty, which will be discussed further in Sec. 6.2.1.

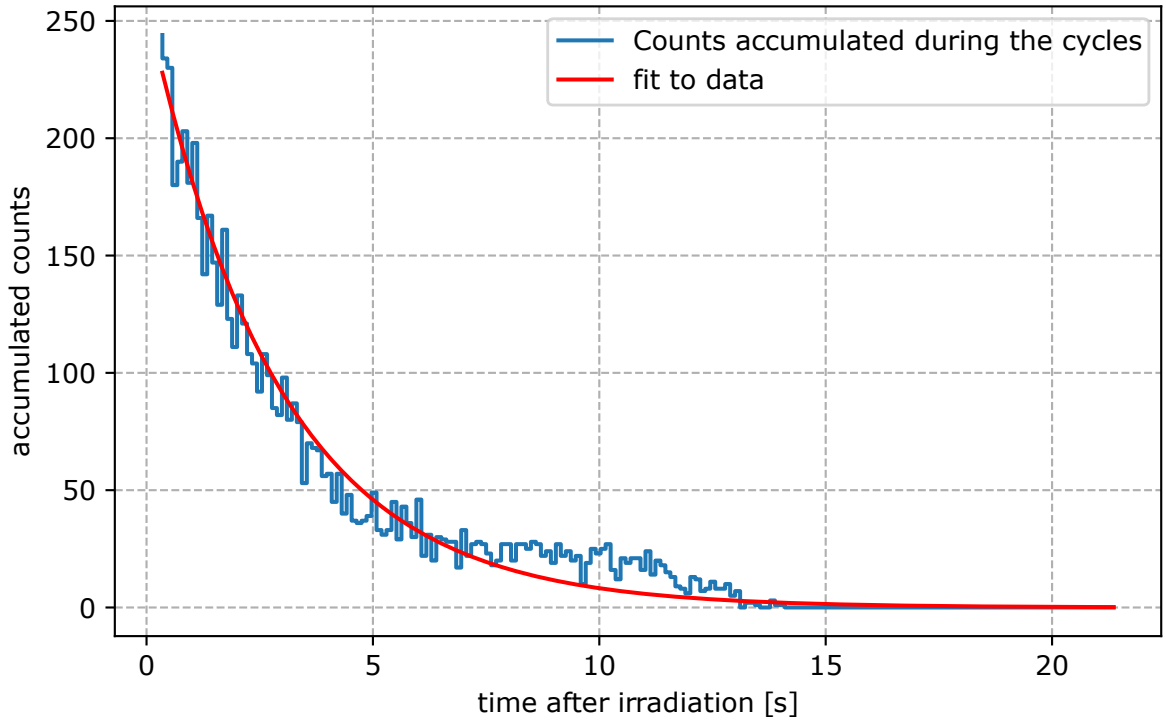

Figure 5.6: Counts within an energy window of 162±2 keV accumulating over a time window of 110 ms summed over all and the exponential fit to this data. The fit coefficients are $\beta = 2.012 \pm 0.0025$ s for the half-life and $A = 257 \pm 16$ counts for the activation factor.

5.2.3 Coincidence analysis

The results for the coincidence analysis are displayed in Fig. 5.7, showing the coincidence matrix within the energy window of 1100 and 1400 keV. The coincidences of different energies are more common than the ones with same energies, which implies that there are some actual coincidence events recorded, even with the detectors only occupying a small fraction of the solid angle in the 90° setup. The spectrum shows a full ^{60}Co spectrum including the Compton continuum, as these events will also happen in coincidence.

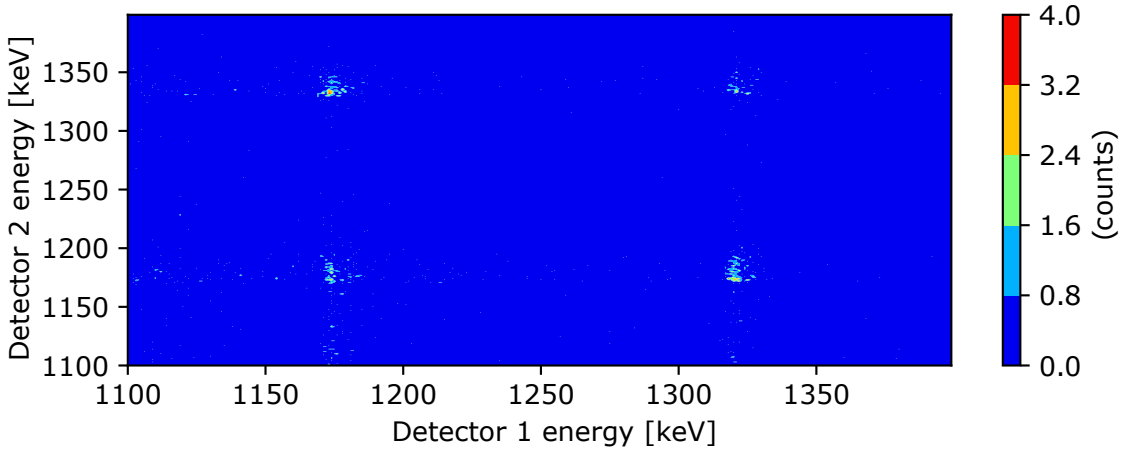

(a) Coincidence matrix in the region between 1100 and 1400 keV. The peaks with different energies show a slightly higher intensity than the ones registering the same energy in the different channels (i.e. random coincidence).

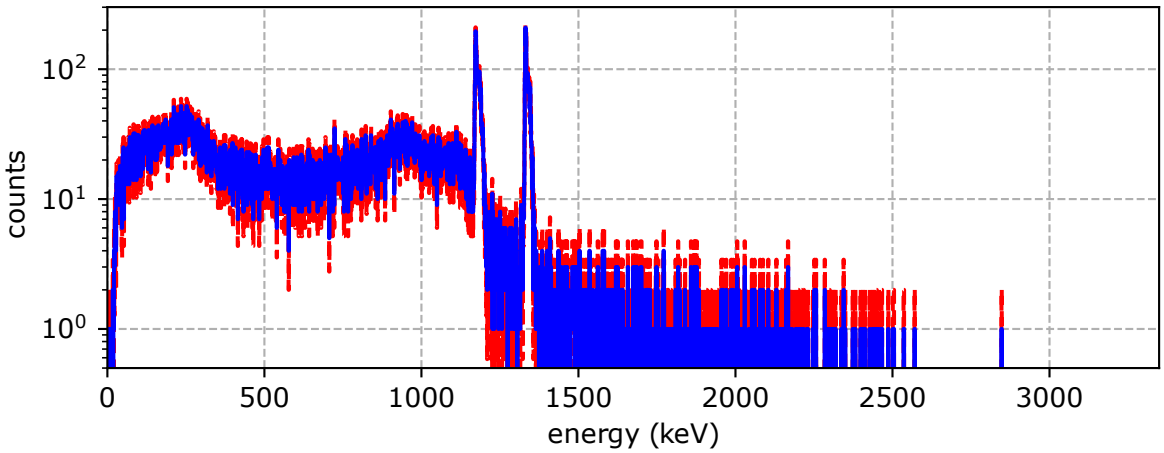

(b) Coincidence spectrum with errors created by projecting the coincidence matrix onto Detector 1.

Figure 5.7: Coincidence analysis of a ^{60}Co-spectrum. The time window used was 500 ns.

6 Discussion

In this section, the results will be thoroughly examined to discuss their validity and significance. The section is divided, first looking at the measurement characterising the properties of the setup and then the measurements regarding the more practical aspects when analysing actual spectra.

6.1 Setup characterisations

The first aspects that will be discussed in this chapter are the aspects of characterising the setup. This includes things like the calibration procedures, the dead-time determination with manually written code comparing to the default inbuilt one. The last two parts in this section discuss the noise level determination and the background measurement.

6.1.1 Energy and efficiency calibration

The first aspect that should be discussed is the energy and efficiency calibration presented in Section 4.1.1. The energy calibration used was a simple linear function, which for HPGe detector in the energy range where the calibration measurements are taken (120 to 1500 keV). The efficiency calibration presented in Section 4.1.1 is using the fit function and scaling principles from [37], regarding the normalisation towards the ^{60}Co peak at 1332 keV. Due to an absence of calibrated sources, the external trigger method would be the desired choice for a very precise measurement of this specific lines efficiency.

The shape of the efficiency curves looks fairly consistent with literature. However, the decline of efficiency towards lower energies can not be seen, which is mainly due to the lack of data points within that region. Thus, there is a need for more points to calibrate to, especially between 20 keV and 100 keV but also above 1400 keV. Using ^{133}Ba on top of ^{152}Eu and ^{226}Ra for the low-energy range and ^{208}Tl for the high end of the spectral range could be something to consider according to [16].

6.1.2 Dead-time correction

Looking at the data in Fig. 4.3, the manually calculated dead-time shows a fairly linear relation compared to the one provided by COMPASS. As COMPASS estimates the dead-time based on certain criteria given in [35], it is hard to say, which version is more accurate without some independent metric. The manual estimation of the dead-time shows an average increase in dead-time of about 50% compared to COMPASS with some exceptions from the Co1 and Eu1 measurements. This works, as long as the count rate from the sample is not higher than 1 GBq. There is something more to be said about the two measurements which show up underneath the equality line. For these measurements the samples were placed

inside of the steel pipe section, the place where the samples are located when running actual measurements. It is not quite clear what causes this phenomenon, it could be a case of the specific location where the samples are placed. This is something that would be interesting to investigate further in a more specifically targeted measurement (see Section 7.2).

6.1.3 Channel noise

Analysing the noise in the channels, Fig. 5.2 shows the exponential fitted to the curve. Using a factor of 3 for multiplying with the absolute value of the noise levels for the fit gives a curve that encloses a sufficient range of values, using a binning of 1 keV per bin. This allows the fit function to serve as a general lower bound of counts that a peak needs to surpass in order to show up in a spectrum. With this it is possible to determine a detection limit for different elements based on the known weight of the sample and the amount of counts that are recorded in the measurements (see Table 5.2). Considering the method by which the data was generated, using 30 second slices over a time of 4 h while the generator was running gives data that is sufficiently symmetric around the energy-axis to justify the approach. The result can therefore be considered white noise from the various possible sources of noise like the detector, the pre-amplifier and the power grid within the facility. The influence of gain shifts, however, is something that also needs to be considered when evaluating the background measurement.

6.1.4 Background measurement

Using the background measurement taken in list mode, this conveniently allows to slice up the background for individual measurements as needed, just taking the time slices when the measurement was running. This allows using one long measurement of 4 h as source to create background for virtually any other measurement in any timing configuration. Using this for the SBR-study showed consistent result, but also brought up limitations. First and foremost, there are the changes in the lab prior to the background measurements but after all other measurements. These consisted of removing a separate experiment, that incorporated a large amount of moderating plastics and roughly 250 kg lead bricks, from between the detectors and the neutron source. This means that the background spectrum shows an artificially increased rate of counts especially from the prompt-gammas like the ^{1}H line at 2223.25 keV which are directly from the shielding material of the generator cave. On the other hand, there will be a decrease of activity from the lines emitted by the activation of lead (e.g. the line at 660 keV). This affected the two detectors differently due to geometry, meaning that Channel-0 was shielded more by the lead from the removed experiment than Channel-1. When correcting the SBR-measurements, presented in Fig. 5.4, it worked reasonably well when using a constant factor for scaling the background counts. The factors used were determined to be 0.67 for Channel-0 and 0.87 for Channel-1. While this works for the SBR-measurements, the results were more variable for the sample analysis with other elements. This is suspected to be caused by the impact of the shielding on different lines in the background, pushing the Hydrogen-line while suppressing the lead. Another thing that needs to be addressed here is the gain correction that was performed for both the background measurement as well as the SBR-measurements and the sample spectra. Slight changes in detector voltage will result in different gain multiplication and thus the same energy ending up in different bins. As long as the voltage is constant during a measurement,

there might only be a slight constant offset compared to the initial calibration determined in Section 4.1.1. However, a subset of measurements was affected by noise on the pre-amplifier of Channel-0 which resulted in peaks being broadened and showing doublet or triplet peaks which can not be mitigated by performing a linear gain correction. These measurements had to be excluded.

6.1.5 SBR-measurements

Looking closely at the measurements presented in Fig. 5.3 and Fig. 5.4, the background without subtraction grows in a linear fashion with increasing measurement time. This implies that the actual background is behaving in a linear fashion, which validates the linear background subtraction. In the background-subtracted spectra, counts outside of the photopeaks are therefore assumed to be due only to Compton background from longer-lived isotopes. The signal consists of the fitted counts within the peak, approaching the limit of the maximal number of counts which can be extracted within the same amount of cycles, which is an expected outcome when measuring an exponential decay. Lastly, as the signal still sits on top of a Compton background from lines with longer half-life (for In in this case), there will still be some background, but it does not necessarily need to be linear any more. These are phenomena we can observe in the plots, but there are also a few things that can be recognised apart from that. For one, there are issues with the 4-half-lives measurements. The two points that are shown in the data appear with a reduction in signal count and an even bigger reduction in background, which seems a bit odd. Both of the good measurements were taken with channel 1. The other two had to be discarded due to aforementioned gain drift during the measurement, rendering the 162 keV-peak into a triplet peak, which will serve the purpose very badly, as it artificially increases the linear area under the fit curve. Another thing that has to be noted is that there is some rate correction going on with a few of the measurements, as some were taken while the generator was not running at full load (10/5 and 5/5 measurement with a flux of 3.5e8). Also the flux at which the generator was run during the 10/10 measurement is not retracable with 100% confidence, which means there is some doubt towards whether the measurements for that point are actually accurate. Overall though, this study gives the notion towards using only the data from the first half-life period of measuring if a maximised SBR is desired. For a more quantitative approach however, it is maybe better to take more than one half-life of measurements as long as the signal still surpasses the noise boundary. Also this measurement served as a test case for the background subtraction including the gain correction, and ultimately, it does show that the background correction definitely does serve its purpose in actually increasing the SBR and cleaning out peaks in the spectra that originate from the background.

6.2 Measurements

This section deals with the data analysis procedures that were performed on data from the setup. This includes half-life analysis of specific lines, the spectral analysis of several different samples, and then lastly the evaluation of the coincidence measurement.

6.2.1 Decay analysis

The line examined for the decay analysis was again the 162 keV line from indium. The short half-life of two seconds and the high strength of this line due to a high production cross-section make it convenient to analyse with the short time window used for integrating the peaks. The best results could be achieved by fitting an exponential decay without constant offset, the coefficients given in Section 5.2.2. This was performed following a background subtraction using the mean of the two adjacent energy windows as described in Section 4.2.6. This yields a result that is within 10% of the literature value of 2.18 s ([41]). With the small fraction of uncertainty on the fit, there is a high chance that the uncertainty is underestimated and the method for uncertainty determination needs further refinement. These results indicate that the general approach is going in the right direction, and with some improvement could reliably determine unknown half-lives. This might also only work for fairly strong lines, this is where some more testing needs to really stretch the method to its limits.

6.2.2 Coincidence analysis

The coincidence analysis was run on a dataset of ^{60}Co, which of course is not an activation product. But the nature of the source having a strength on the order of hundreds of MBq and also emitting the two gamma-rays of 1173 keV and 1332 keV almost every time in coincidence will help a lot in seeing any coincidence. The problem here is that the solid angle Ω of one detector is only 0.91 sr at the distance they are placed from the source. This means the spectrum will condense down a lot when applying the coincidence matrix and it is down to a few coincident events that show up when plotting the matrix (see Fig. 5.7). However, the fact that the peaks on the off-diagonal are stronger than the peaks showing two same-energy events hints towards the fact that there are indeed some coincident events, whereas the same-energy peaks should give an estimate on the amount of random coincidences happening. This was only really a test-run to show that the setup is capable of doing this kind of analysis, but if applied to some of the single-sample measurements, or even some mixed-samples, this could provide the possibility for pushing the detection limits (see Table 5.2) far down, as it will reduce all the background even more. For this purpose the acquisition mode within COMPASS should be changed as well, to optimise for the coincident events. With the single event mode the time resolution of 10 ns is not good enough to study events with sub-ns coincidences.

6.2.3 Spectral analysis

For the analysis of the spectra, the fit coefficients for all the peaks that were fitted are presented in Table B.1. Looking at the different aspects of these fits, the energy fitting does match up with the line of the energy of the emission within a deviation of up to 2 keV. This is bigger than the error on the energy fit, but can be explained with the gain shift correction not performing perfectly for some samples, and thus also the background subtraction affecting slightly wrong channels. Looking at the fit values for σ, having a value of around 1 keV gives a FWHM of roughly 2.335 keV. This means that the peaks still span over 3-4 bins and there is no necessity to go towards finer binning, which could increase the influence of noise fluctuations in the bins. The last fit parameter is the peak area. When evaluating the

fits to the peak area, there is a noticeable difference compared to the other fit parameters, regarding the uncertainty. Here the uncertainty is at least on the order of the fitted value, if not (much) bigger. To understand this circumstance, it is important to keep in mind, that the fit is still performed on top of a linear background. Therefore the uncertainties from the background measurements fold in to the fit uncertainty. The variable success with the different samples regarding the background subtraction also comes into play here. Lastly there is still a possibility that the fit algorithm could not locate the desired peak, as not all peaks show up to the same extent in the two different channels. Overall, this means that while the quantitative determination of sample material can be challenging, the qualitative analysis of a NAA spectrum is definitely possible and provides sensitivities down towards the mg regime using only the low-flux neutron generator which is considerably smaller than usual reactor neutron flux used for NAA.

7 Summary and outlook

Considering the initial purpose of this work, which was in improving and automating the system and testing its capabilities, the project can be stated as a success overall. The measurements can now be set up to run in an automated fashion, and the detection limits for 5 different samples could be determined. There is still room for improvement, but the system in general works as a prototype of a cyclic NAA setup. Within the greater scheme of ultimately determining the viability for detecting small concentrations of ^{148}Gd within environmental samples, there is still a long way to go though.

7.1 Conclusions

The system provides a number of possible ways to analyse data, ranging from simple spectral analysis up to determining the decay constants of specific lines (given some polishing) and running coincidence analysis on the spectra using the two different detectors. To be a bit more specific, the findings of this study are summarised in the following list:

- capability to observe short-lived isotopes down to sub-second half-lives
- detection limits down to the order of mg as of now
- setup can run independently after starting the measurement
- adjustable irradiation, measurement and cooldown
- decay- and coincidence analysis are possible

This marks a promising step on the way towards the later integration of this method into the planned CANS-based setup under construction. The self-imposed boundary of 2 h of maximum measurement time had an effect as well resulting in no measurable signal mostly for longer lived isotopes (few cycles) which did not show a particularly high cross-section (thus low signal in general). Examples that can be mentioned here are Tungsten, Silver and Iridium. The detection limits that could be possible when used with the CANS are not easy to estimate, as there are a number of factors at play. First of all, there is an overall increase in neutron flux by a factor of 10^3, which should scale linearly towards the detection limit. Secondly, the geometry of the setup will change drastically, and depending on where the detector setup is placed, there could be a significant decrease in neutron background, also improving the detection limits by some factor. Lastly there is also the possibility of using an entirely different set of detectors and together with coincidence analysis this could drastically improve the detection limits as well. So in conclusion, the work performed within the scope of this project can be considered a step in the right direction, and shows that there is a lot of potential with this setup especially by inclusion into the CANS setup. There is also a lot of things that can be addressed in future work, which is presented in the following.

7.2 Future work

Within the process of this work, a list of things that showed potential for improvement was collected, and will be presented here. The first thing that will be discussed regards the changes that can be directly implemented within the current setup. During the measurements there were a considerable amount of measurements (especially with heavy samples like Pb) where the sample container shattered because of the impact when hitting the end of the pressure line with enough impact. Therefore it is proposed to add some padding on both ends, as well as potentially commissioning sample holders from a different material and out of one solid piece, as the 3D-print does not withstand the stress it is exposed to. The padding however has to be a material that can withstand high impacts, while at the same time finding the right compromise between dampening the impact and being too elastic, such that the sample does not come to rest at the desired position but be bounced back. The implementation into the CANS-setup is an obvious piece of future work, as this was already the initial prospect of this prototype. Adding improvements there by exchanging the detector setup is not necessarily a requirement, but is a possibility if better resolution or efficiency is desired. Another improvement would be an efficiency calibration measurement using the external trigger method as described in [37], which would help with quantifying the results of the spectral measurements. The list mode data acquisition can also be configured to always measure the full time of 10 half-lives and then choosing the best interval in post-processing of the data, so that the time is used in the most optimised fashion.

There is also a list of measurements that are possible to understand the setup in more depth. These could be:

- measuring more samples with known mixed constitution
- measuring samples with long half-lives with potential cooldown periods before measurement
- performing specific coincidence measurements with NAA samples
- performing quantitative analysis of sample materials
- generally measuring a wider set of samples
- detailed comparisons for background measurements with a a constant lab environment

Overall there is a lot of potential for future work, the extent of the individual tasks providing a wide variety of possible projects.

Acknowledgements

First and foremost, I want to thank my supervisor, Robert Frost, for all the work and time he spent with me in the lab, doing our best to get this setup to the state it is in now. His suggestions always turned out worth the time spending on implementing them. He also pushed me continuously to work more and more on my own, giving me a valuable learning experience. His feedback, together with the feedback from Kristina Eriksson-Stenström, helped me a lot improving the report to get it into the final shape.

Additionally there are a few people within the Nuclear Physics department I want to mention here. Mikael Elfman for helping me find my way around the lab, Daniel Cox for providing insight into calibration procedures and all the other people for creating a friendly and welcoming atmosphere to work in.

Funding was provided by the Swedish Radiation Safety Authority (grant SSM2021-787) and the Walter Gyllenberg foundation. The Neutron generator was provided by SKB (Swedish Nuclear Fuel and Waste Management Company).

Last, but not least, I want to thank my partner and family for providing me backup during the most stressful times.

References

[1] E. Witkowska, K. Szczepaniak, M. Biziuk. Some applications of neutron activation analysis. *Journal of Radioanalytical and Nuclear Chemistry*, vol. 265 (2005), 141–150. doi: 10.1007/s10967-005-0799-1

[2] S. Goderis, H. Sato, L. Ferrière, *et al.* Globally distributed iridium layer preserved within the Chicxulub impact structure. *Science Advances*, vol. 7 (2021). doi: 10.1126/sciadv.abe3647

[3] J. Yellin. Neutron activation analysis: impact on the archaeology of the Holy Land. *TrAC Trends in Analytical Chemistry*, vol. 14 (1995), 37–44. doi: 10.1016/0165-9936(95)91144-h

[4] J. Lilley. Neutron activation analysis, chap. 8.4, In *Nuclear Physics Principles and Applications*. Wiley (2001)

[5] W. Rosenstock, T. Köble, M. Risse, W. Berky. Detection of Concealed Fissionable Material by Delayed Neutron Counting (2009)

[6] S. Boschi, B. Schmitz, F. Terfelt, *et al.* Popigai impact ejecta layer and extraterrestrial spinels recovered in a new Italian location - The Monte Vaccaro section (Marche Apennines, Italy), In *250 Million Years of Earth History in Central Italy: Celebrating 25 Years of the Geological Observatory of Coldigioco*. Geological Society of America (2019). ISBN 9780813725420. doi: 10.1130/2019.2542(19)

[7] H. Perrey, M. Elfman, K. Fissum, *et al.* From micro- to macro- neutron sources: The Lund Broad-band Neutron Facility. *EPJ Web Conf.*, vol. 231 (2020), 01005. doi: 10.1051/epjconf/202023101005

[8] M. Kristensson. Characterisation of a neutron experimental station at the Lund Ion Beam Analysis Facility (2018). URL `http://lup.lub.lu.se/student-papers/record/8962519`. Master's thesis

[9] J. Lindsey-Clark. Development of a Neutron Activation Analysis station at the Lund Ion Beam Analysis Facility. Lund University (2021). URL `http://lup.lub.lu.se/student-papers/record/9038694`. Student Paper

[10] K. Eriksson Stenström, V. Barkauskas, G. Pédehontaa-Hiaa, *et al.* Identifying radiologically important ESS-specific radionuclides and relevant detection methods. Tech. rep., Strålsäkerhetsmyndigheten (2020)

[11] V. Barkauskas, K. Stenström. Prediction of the radionuclide inventory in the European Spallation Source target using FLUKA. *Nuclear Instruments and Methods in Physics Research Section B: Beam Interactions with Materials and Atoms*, vol. 471 (2020), 24–32. doi: 10.1016/j.nimb.2020.03.013

[12] K. Eckerman, J. Harrison, H.-G. Menzel, C. Clement. ICRP Publication 119: Compendium of Dose Coefficients based on ICRP Publication 60. *Annals of the ICRP*, vol. 42 (2013), e1–e130. doi: 10.1016/j.icrp.2013.05.003

[13] M. J. T. Milton, T. J. Quinn. Primary methods for the measurement of amount of substance. *Metrologia*, vol. 38 (2001), 289–296. doi: 10.1088/0026-1394/38/4/1

[14] R. R. Greenberg, P. Bode, E. A. D. N. Fernandes. Neutron activation analysis: A primary method of measurement. *Spectrochimica Acta Part B: Atomic Spectroscopy*, vol. 66 (2011), 193–241. doi: 10.1016/j.sab.2010.12.011

[15] D. Soete, R. Gijbels, J. Hoste. Neutron Activation Analysis, vol. 34 of *Chemical analysis : a series of monographs on analytical chemistry and its applications*, chap. 4.II. Wiley-Interscience (1972)

[16] G. F. Knoll. Germanium gamma-ray detectors, chap. 2, In *Radiation Detection and Measurement*. Wiley (2010)

[17] R. Frost (2022). Private communication

[18] J.-C. Sublet, J. Eastwood, J. Morgan, *et al.* FISPACT-II: An Advanced Simulation System for Activation, Transmutation and Material Modelling. *Nuclear Data Sheets*, vol. 139 (2017), 77–137. doi: 10.1016/j.nds.2017.01.002

[19] K. S. Krane, D. Halliday. Introductory nuclear physics, chap. 12. Wiley, New York, 2. ed. ed. (1988)

[20] J.-L. Basdevant, J. Rich, M. Spiro. Fundamentals in Nuclear Physics: From Nuclear Structure to Cosmology, chap. 3, 167–169. Springer Nature (2005)

[21] J. Chadwick. Possible Existence of a Neutron. *Nature*, vol. 129 (1932), 312–312. doi: 10.1038/129312a0

[22] P. Ring, P. Schuck. The Nuclear Many-Body Problem, chap. 1. Springer-Verlag GmbH (2004)

[23] H. A. Bethe, R. F. Bacher. Nuclear Physics A. Stationary States of Nuclei. *Reviews of Modern Physics*, vol. 8 (1936), 82–229. doi: 10.1103/revmodphys.8.82

[24] C. F. v. Weizsäcker. Zur Theorie der Kernmassen. *Zeitschrift für Physik*, vol. 96 (1935), 431–458. doi: 10.1007/bf01337700

[25] K. S. Krane, D. Halliday. Introductory nuclear physics, chap. 12.4, 456 – 462. Wiley, New York, 2. ed. ed. (1988)

[26] X. Hou. Activation analysis for the determination of long-lived radionuclides. *Radioactivity in the Environment* (2008), 371–405. doi: 10.1016/S1569-4860(07)11012-3

[27] F. De Corte. The k0-standardization Method. A Move to the Optimization of Neutron Activation Analysis (1987)

[28] F. D. Corte. The standardisation of standardless NAA. *Journal of Radioanalytical and Nuclear Chemistry*, vol. 248 (2001), 13–20. doi: 10.1023/a:1010601403010

[29] F. D. Corte, A. Simonits. Recommended nuclear data for use in the k0 standardization of neutron activation analysis. *Atomic Data and Nuclear Data Tables*, vol. 85 (2003), 47–67. doi: 10.1016/s0092-640x(03)00036-6

[30] G. F. Knoll. Radiation interactions, chap. 12, 48 – 52, In *Radiation Detection and Measurement*. Wiley (2010)

[31] Autodesk. Fusion360. CAD Software (2020). © Autodesk Inc.

[32] M. Elfman, J. Pallon. personal communication (2021)

[33] B. A. G. . C. KG. TwinCAT 3 Engineering (2021). Version 3.1,Build 4024.28

[34] CAEN Electronic Instr. CoMPASS - Multiparametric DAQ Software for Physics applications (2021)

[35] UM5690 User Manual. *CoMPASS - Multiparametric DAQ Software for Physics applications*. CAEN Electronic Instrumentation, 14 ed. (2021)

[36] CAEN Electronic Instr. Personal communication (2022)

[37] N. Lalović, C. Louchart, C. Michelagnoli, *et al.* Performance of the AGATA γ-ray spectrometer in the PreSPEC set-up at GSI. *Nuclear Instruments and Methods in Physics Research Section A: Accelerators, Spectrometers, Detectors and Associated Equipment*, vol. 806 (2016), 258–266. doi: https://doi.org/10.1016/j.nima.2015.10.032

[38] R. Brun, F. Rademakers, P. Canal, *et al.* root-project/root: v6.18/02 (2019). doi: 10.5281/ZENODO.3895860. ROOT package and PyROOT implementation

[39] D. Radford. ESCL8R and LEVIT8R: Software for interactive graphical analysis of HPGe coincidence data sets. *Nuclear Instruments and Methods in Physics Research Section A: Accelerators, Spectrometers, Detectors and Associated Equipment*, vol. 361 (1995), 297–305. doi: 10.1016/0168-9002(95)00183-2

[40] UM6771 User Manual. *780 DPP_PHA*. CAEN Electronic Instrumentation (2020)

[41] Lund/LBNL Nuclear Data Search (2022). URL `http://nucleardata.nuclear.lu.se/toi/`

[42] Neutron Generators for Analytical Purposes. Tech. rep., Intl Atomic Energy Agency (2012)

[43] M. Dayah. Periodic Table - Ptable (1997). URL `https://ptable.com`. Accessed 30/04/2022

[44] D. Brown, M. Chadwick, R. Capote, *et al.* ENDF/B-VIII.0: The 8 th Major Release of the Nuclear Reaction Data Library with CIELO-project Cross Sections, New Standards and Thermal Scattering Data. *Nuclear Data Sheets*, vol. 148 (2018), 1–142. doi: 10.1016/j.nds.2018.02.001

Appendices

Table of observable reactions within the used samples

Table A.1: Table of delayed gamma emission after neutron activation. Compiled from: [42, 43] (reaction and abundance), the ENSDF library via [41](half-life, lines and rel. intensity) and the ENDF/B VIII.0 dataset [44] (cross-sections)

Reaction	abund. (%)	σ_{Th} (mb)	σ_{3} (mb)	$\sigma_{14.1}$ (mb)	HL	lines(keV)	I(%)
^{23}Na(n,γ)^{24}Na	100	528.2	0.17	0.21	14.95 h	1368.633	100
						2754.028	99.944
^{23}Na(n,α,γ)^{20}F	100	-	-	138.2	11.0 s	1633.602	100
^{27}Al(n,γ)^{28}Al	100	233.5	0.42	0.63	134.484 s	1778.969	100
^{27}Al(n,aγ)^{24}Na	100			120.8	14.95 h	1368.633	100
						2754.028	99.944
^{27}Al(n,p)^{27}Mg	100	-	1.1	72.0	9.46 m	843.74	71.8
						1014.42	28.0
^{28}Si(n,p)^{28}Al	92.2	-	-	276.5	134.484 s	1778.969	100
^{30}Si(n,γ)^{31}Si	3.09	107.1	0.65	0.61	157 m	1266.12	0.07
^{37}Cl(n,γ)^{38m}Cl	24	433.1	0.55	0.55	0.715 s	671.355	99.95
^{37}Cl(n,γ)^{38m}Cl	24	433.1	0.55	0.55	37.2 m	2167.405	42.4
						1642.714	31.9
^{54}Fe(n,2n)^{53}Fe	5.84	-	-	1.62	8.51 m	377.88	42
^{56}Fe(n,γ)^{56}Mn	91.75	-	3.5e-11	114.1	2.58 h	846.771	98.9
						1810.772	27.2
						2113.123	14.3
						2522.88	0.99
^{54}Cr(n,γ)^{55}Cr	2.37	411.2	0.88	0.55	3.50 m	126.0	4.7
						1402.0	3.6
						1528.01	100
						2240.9	1.07
						2252.5	8.5
^{52}Cr(n,p)^{52}V	83.79	-	-	89	3.74 m	1434.068	100
^{55}Mn(n,α,γ)^{52}V	100	-	-	1.3	3.74 m	1434.068	100
^{55}Mn(n,p)^{55}Cr	100	-	0	45.3	3.50 m	126.0	4.7
						1402.0	3.6
						1528.01	100
						2240.9	1.07
						2252.5	8.5
^{55}Mn(n,γ)^{56}Mn	100	13279.0	1.3	6.2e-4	2.58 h	846.771	98.9
						1810.772	27.2
						2113.123	14.3
						2522.88	0.99

Reaction	abund. (%)	σ_{Th} (mb)	σ_{3} (mb)	$\sigma_{14.1}$ (mb)	HL	lines(keV)	I(%)
^{58}Ni(n,n'p)^{57}Co	68.08	-	-	571.6	271.8 d	122.0614	85.6
						136.4743	10.68
^{60}Ni(n,p)^{60m}Co	26.22	-	6.9e-5	159.3	10.467 m	58.603	2.0
^{64}Ni(n,γ)^{65}Ni	0.93	1480.4	1.00	0.51	2.52 h	366.27	4.81
						1115.546	15.43
						1481.84	24
^{73}Ge(n,n'γ)^{73m}Ge	7.73	-	1964	280	0.499 s	53.440	10.34
^{74}Ge(n,γ)^{75}Ge	36.28	519	2.665	4659	82.8 m	198.6060	1.19
						264.6576	11
^{76}Ge(n,2n)^{75m}Ge	36.28	-	-	1163.7	47.700 s	139.68	39
^{76}Ge(n,γ)^{77m}Ge	9.37	154.6	13.6	4292	52.900 s	159.7	10.33
						215.51	21.4
^{90}Zr(n,n'γ)^{90}Zr	51.45	-	1267.16	873.93	0.809 s	133.0	???
						2180.0	
						2315.0	
^{90}Zr(n,n'p)^{89m}Y	51.45	-	-	247.56	16.06 s	908.96	99
^{90}Zr(n,2n)^{89m}Zr	51.45	-	-	587.7	4.16 m	587.83	90
						1507.11	6.06
^{90}Zr(n,p)^{90}Y	51.45	-	2.14e-4	35.82	64.05 h	beta	99.9885
^{96}Zr(n,γ)^{97}Zr	2.80	20.32	4.16	0.56	16.7 h	254.17	1.14
						355.40	2.09
						507.64	5.03
						602.37	1.38
						703.76	1.01
						743.36	93
						1021.2	1.01
						1147.97	2.61
						1362.68	1.02
						1750.24	1.09
^{107}Ag(n,n'γ)^{107m}Ag	51.84	-	2023.9	367.8	44.5 s	93.124	4.7
^{107}Ag(n,γ)^{108}Ag	51.84	37604.8	51.35	7.84e-5	2.4 m	632.97	1.76
^{109}Ag(n,α)^{106}Rh	48.16	-	9.5e-9	4.3	29.8 s	621.94	9.93
						1050.39	1.56
^{109}Ag(n,n'γ)^{109m}Ag	48.16	-	2186.1	479.7	39.6 s	88.04	3.66
^{109}Ag(n,γ)^{110}Ag	48.16	90265.9	26.2	1.8e-4	24.6 s	657.7622	4.5
^{113}In(n,γ)^{114}In	4.29	-	63.5	1.00	71.900 s	beta	99.5
^{113}In(n,n'γ)^{113m}In	4.29	12134.9	1850.4	549.0	99.5 m	391.690	64.2
^{115}In(n,γ)^{116}In	95.71	202275	66.9	1.02	14.100 s	1293.558	1.3
^{115}In(n,γ)^{116m1}In	95.71	202275	66.9	1.02	54.3 m	138.33	3.29
						416.86	27.7
						828.72	11.5
						1097.33	56.2
						1293.56	84.4
						1507.67	10.0
						11752.72	2.46
						2112.3	15.5
^{115}In(n,γ)^{116m2}In	95.71	202275	66.9	1.02	2.180 s	162.393	37.2

Reaction	abund. (%)	σ_{Th} (mb)	σ_3 (mb)	$\sigma_{14.1}$ (mb)	HL	lines(keV)	I(%)
^{115}In(n,n'γ)^{115m}In	95.71	-	1820.5	211.6	4.49 h	336.240	45.8
^{115}In(n,aγ)^{112}Ag	95.71	-	1.13e-7	2.10	3.13 h	606.88	3.1
						692.70	1.08
						694.863	3.0
						851.10	1.03
						1312.29	1.20
						1387.67	5.4
						1613.57	2.8
						2106.16	2.4
						2506.80	1.08
^{158}Gd(n,γ)^{159}Gd	24.84	2202.6	23.7	1.16	18.48 h	58.00	2.1
						363.55	11.4
^{160}Gd(n,γ)^{161}Gd	21.86	1410.3	7.85	0.97	3.66 m	56.290	5.95
						77.393	1.06
						102.315	22.7
						165.213	2.58
						283.55	13.9
						314.92	3.77
						338.07	1.68
						360.94	60.1
						480.12	2.68
						529.50	1.26
^{178}Hf(n,n'γ)^{178m}Hf	27.28	-	3432.50	488.35	4.000 s	88.867	64.4
						93.180	17.2
						213.440	81.4
						325.562	94.1
						426.383	94.1
							97.0
^{179}Hf(n,n'γ)^{179m}Hf	13.63	-	3133.11	300.86	18.670 s	160.696	2.78
						214.335	94
^{180}Hf(n,n'γ)^{180m}Hf	35.08	-	3493.39	464.35	5.47 h	57.555	48.0
						93.326	17.1
						215.256	81.3
						332.277	94.1
						443.09	81.9
						500.64	14.3
^{182}W(n,γ)^{183m}W	26.50	20315	33.6	0.71	5.200 s	46.4839	6.13
^{183}W(n,n'γ)^{183m}W	14.31	-	3275.2	437.5		52.5954	6.76
						99.0792	8.14
						102.481	2.42
						107.9322	18.9
						160.5276	5.12
^{184}W(n,γ)^{185m}W					100.200 s	65.86	5.8
						131.55	4.33
						173.68	3.26

Reaction	abund. (%)	σ_{Th} (mb)	σ_3 (mb)	$\sigma_{14.1}$ (mb)	HL	lines(keV)	I(%)
^{186}W(n,γ)^{187}W	28.42	37893.7	18.3	1.39	23.7 h	72.001	11.14
						134.243	8.85
						479.531	21.8
						551.532	5.08
						618.361	6.28
						625.511	1.089
						685.774	27.5
						772.89	4.12
^{191}Ir(n,2n)^{190}Ir	37.3	-	-	962.7	11.78 d	186.718	52.4
						361.136	13.0
						371.260	23.0
						407.176	23.9
						518.55	34.0
						557.972	30.1
						569.310	28.5
						605.24	39.9
^{191}Ir(n,2n)^{190m}Ir	37.3	-	-	345.7	3.09 h		
^{191}Ir(n,2n)^{190m2}Ir	37.3	-	-	745.4	3.09 h	186.718	66.3
						361.136	89.57
						502.53	92.31
						616.08	93.10
^{191}Ir(n,n'γ)^{191m1}Ir	37.3	-	2854.0	331.6	4.940 s	129.421	29.0
^{191}Ir(n,n'γ)^{191m2}Ir					5.5 s	414.3	24
						586.5	76
^{191}Ir(n,γ)^{192m}Ir	37.3	954263.6	66.6	1.88	87.0 s	56.68	0.034
^{193}Ir(n,2n)^{192m}Ir	62.7	-	-	166		295.958	*
						316.508	*
						612.466	*
^{193}Ir(n,2n)^{192}Ir	62.7	-	-	2009.1	87.0 s	205.795	3.30
						295.958	28.69
						308.457	30.00
						316.508	83.83
						468.072	47.83
						484.578	3.18
						588.585	4.51
						604.415	8.23
						612.466	5.31
^{193}Ir(n,n'γ)^{193m}Ir	62.7	-	2823.1	307.8	5.5 s	180.236	0.0047
^{193}Ir(n,γ)^{194}Ir	62.7	111168.3	30.3	0.94	19.28 h	293.545	2.52
						328.455	13.1
						645.157	1.18
^{197}Au(n,α)^{194}Ir	100	-	5e-13	2.5e-4	19.28 h	293.545	2.52
						328.455	13.1
						645.157	1.18
^{197}Au(n,2n)^{196}Au	100	-	-	2122	6.18 d	332.983	22.9
						355.684	87
						426.0	7

Reaction	abund. (%)	$\boldsymbol{\sigma_{Th}}$ (mb)	$\boldsymbol{\sigma_{3}}$ (mb)	$\boldsymbol{\sigma_{14.1}}$ (mb)	HL	lines(keV)	I(%)
^{197}Au(n,2n)^{196m2}Au	100	-	-	2122	9.6 h	137.69	1.5
						147.81	43
						168.37	5.9
						188.27	34.0
						285.49	4.0
						316.19	2.80
^{197}Au(n,p)^{197m}Pt	100	-	5e-13	1.8	95.41 m	53.10	1.09
						279.01	2.4
						346.5	11.1
^{197}Au(n,p)^{197}Pt	100	-	5e-13	1.8	19.28 h	77.351	17.0
						191.437	3.7
^{197}Au(n,n'γ)^{197m}Au	100	-	2626.3	541.4	7.73 s	130.2	3.12
						201.6	1.13
						279.01	71
^{197}Au(n,γ)^{198}Au	100	98.70	24.8	1.32	44.5 s	411.80205	96
^{204}Pb(n,n'γ)^{204m}Pb	1.4	-	2407.0	304.0	1.14 h	374.72	89
						899.15	99
						911.78	90.69
^{206}Pb(n,γ)^{207m}Pb	24.1	29.8	0.48	1.08	0.806 s	569.702	97.87
^{207}Pb(n,n'γ)^{207m}Pb	22.1	-	1873.0	316.3	0.806 s	1063.662	88.5
^{207}Pb(n,γ)^{208}Pb	22.1	712.15	2.16	1.29	prompt	2614.53	99
^{208}Pb(n,γ)^{209}Pb	52.4	0.23	1.1	1.1	3.25 h	beta	100

Table of peaks fitted in the sample spectra.

Table B.1: Table of the fitted peaks within the background-corrected spectra.

Sample/ Reaction	Energy (keV)	E_{err}	σ	σ_{err}	peak area	peak$_{err}$
NaCl	Channel0					
^{23}Na(n,α,γ)^{20}F	1634.07	2.08e-03	1.04e+00	2.06e-03	532	4.08e+02
NaCl	Channel1					
^{23}Na(n,α,γ)^{20}F	1634.14	2.88e-03	1.12e+00	2.88e-03	498	4.27e+02
Germanium	Channel0					
^{73}Ge(n,n'γ)^{73m}Ge	53.47	2.90e-01	9.86e-01	2.97e-01	253	1.44e+04
^{76}Ge(n,2n)^{75m}Ge	140.28	1.33e-03	6.19e-01	1.57e-03	1901	7.61e+03
^{74}Ge(n,γ)^{75}Ge	198.52	1.25e+04	2.84e-01	4.68e+05	304	2.24e+12
^{74}Ge(n,γ)^{75}Ge	262.18	1.69e+00	2.66e+00	1.69e+00	363	2.35e+04
Germanium	Channel1					
^{76}Ge(n,2n)^{75m}Ge	140.21	1.01e-03	6.44e-01	8.31e-04	1974	5.73e+03
^{74}Ge(n,γ)^{75}Ge	194.00	2.33e+15	1.52e-01	3.64e+13	-22	7.23e+17
^{74}Ge(n,γ)^{75}Ge	261.39	6.73e-01	9.90e-01	6.84e-01	-117	7.12e+03
Indium	Channel0					
^{115}In(n,γ)^{116m2}In	162.91	1.72e-04	6.06e-01	8.11e-05	5374	6.89e+03
^{115}In(n,γ)^{116m1}In	417.41	1.38e-04	7.16e-01	2.33e-04	3177	2.38e+03
^{115}In(n,γ)^{116m1}In	1097.66	1.46e-04	9.47e-01	1.50e-04	3448	1.47e+03
^{115}In(n,γ)^{116}In	1294.01	2.26e-04	1.00e+00	2.22e-04	4300	3.11e+03
^{115}In(n,γ)^{116m1}In						
^{115}In(n,γ)^{116m1}In	1507.99	5.22e-03	1.20e+00	5.22e-03	537	7.89e+02
^{115}In(n,γ)^{116m1}In	2112.56	7.15e-03	1.52e+00	7.15e-03	508	5.95e+02
Indium	Channel1					
^{115}In(n,γ)^{116m2}In	162.88	8.45e-05	6.04e-01	4.26e-05	7225	6.15e+03
^{115}In(n,γ)^{116m1}In	417.33	1.54e-04	7.30e-01	1.96e-04	3794	3.27e+03
^{115}In(n,γ)^{116m1}In	1097.72	5.69e-04	9.92e-01	5.71e-04	3630	5.72e+03
^{115}In(n,γ)^{116}In	1293.96	3.15e-04	1.07e+00	3.13e-04	4786	4.71e+03
^{115}In(n,γ)^{116m1}In						
^{115}In(n,γ)^{116m1}In	1508.18	3.70e-03	1.04e+00	3.68e-03	471	5.70e+02
^{115}In(n,γ)^{116m1}In	2112.92	6.64e-03	1.28e+00	6.64e-03	472	6.82e+02
Gd2O3	Channel0					
^{160}Gd(n,γ)^{161}Gd	281.09	1.21e+00	1.00e+00	1.19e+00	123	1.36e+04
^{158}Gd(n,γ)^{159}Gd	360.76	2.29e-02	7.24e-01	2.21e-02	444	6.14e+03
^{160}Gd(n,γ)^{161}Gd						
Gd2O3	Channel1					
^{158}Gd(n,γ)^{159}Gd	360.52	6.59e+06	2.45e-01	3.28e+08	768	3.26e+16
^{160}Gd(n,γ)^{161}Gd						
Hafnium	Channel0					

Table B.1: Table of the fitted peaks within the background-corrected spectra.

Sample/ Reaction	Energy (keV)	E_{err}	σ	σ_{err}	peak area	peak$_{err}$
^{179}Hf(n,n'γ)^{179m}Hf	161.01	8.85e-03	6.11e-01	3.75e-03	1393	2.38e+04
^{178}Hf(n,n'γ)^{178m}Hf	214.54	1.26e-05	6.42e-01	4.20e-05	58319	1.10e+05
^{179}Hf(n,n'γ)^{179m}Hf						
^{180}Hf(n,n'γ)^{180m}Hf						
^{178}Hf(n,n'γ)^{178m}Hf	325.84	8.96e-03	6.94e-01	6.58e-03	526	3.31e+03
^{178}Hf(n,n'γ)^{178m}Hf	426.57	3.34e-03	6.58e-01	8.47e-03	459	1.55e+03
Hafnium	Channel1					
^{179}Hf(n,n'γ)^{179m}Hf	160.89	1.80e-02	6.09e-01	9.14e-03	1396	5e+04
^{178}Hf(n,n'γ)^{178m}Hf	214.67	2.81e-05	6.37e-01	4.57e-05	63040	1.99e+05
^{179}Hf(n,n'γ)^{179m}Hf						
^{180}Hf(n,n'γ)^{180m}Hf						
^{178}Hf(n,n'γ)^{178m}Hf	325.73	5.47e-03	6.07e-01	6.16e-03	491	2.03e+03
^{178}Hf(n,n'γ)^{178m}Hf	426.80	7.67e-03	8.14e-01	7.19e-03	522	2.30e+03
Gold	Channel0					
^{197}Au(n,n'γ)^{197m}Au	279.50	3.33e-02	7.23e-01	6.06e-02	136	1.07e+03
Gold	Channel1					
^{197}Au(n,n'γ)^{197m}Au	279.86	1.99e+00	1.63e+00	1.99e+00	68	2.58e+03
Steel	Channel0					
^{56}Fe(n,γ)^{56}Mn	847.54	5.51e-03	1.57e+00	5.51e-03	9422	1.49e+05
^{55}Mn(n,γ)^{56}Mn						
^{52}Cr(n,p)^{52}V	1434.63	4.38e-03	1.57e+00	4.38e-03	1694	3.83e+03
^{55}Mn(n,α,γ)^{52}V						
^{27}Al(n,γ)^{28}Al	1778.97	8.92e-02	2.15e+00	8.92e-02	319	1.48e+03
^{56}Fe(n,γ)^{56}Mn	1810.90	1.39e-02	1.59e+00	1.39e-02	1375	7.76e+03
^{55}Mn(n,γ)^{56}Mn						
^{56}Fe(n,γ)^{56}Mn	2113.37	9.49e-03	1.79e+00	9.49e-03	730	1.19e+03
^{55}Mn(n,γ)^{56}Mn						
Steel	Channel1					
^{56}Fe(n,γ)^{56}Mn	847.49	3.21e-04	9.14e-01	3.42e-04	8066	1.92e+04
^{55}Mn(n,γ)^{56}Mn						
^{52}Cr(n,p)^{52}V	1434.57	2.36e-03	1.16e+00	2.37e-03	1402	2.58e+03
^{55}Mn(n,α,γ)^{52}V						
^{27}Al(n,γ)^{28}Al	1779.18	2.64e-02	1.02e+00	2.62e-02	215	8.88e+02
^{56}Fe(n,γ)^{56}Mn	1811.15	1.00e-02	1.20e+00	1.00e-02	1064	5.91e+03
^{55}Mn(n,γ)^{56}Mn						
^{56}Fe(n,γ)^{56}Mn	2113.42	6.44e-03	1.08e+00	6.46e-03	503	1.04e+03
^{55}Mn(n,γ)^{56}Mn						
Soil_short	Channel0					
^{56}Fe(n,γ)^{56}Mn	844.81	-6.36e+12	1.30e-01	-2.80e+11	85	-8.45e+18
^{27}Al(n,γ)^{28}Al	1779.49	2.87e-03	1.56e+00	2.87e-03	3482	1.08e+04
Soil_short	Channel1					
^{56}Fe(n,γ)^{56}Mn	846.47	7.50e+06	2.54e-01	1.23e+08	-195	5.70e+14
^{27}Al(n,γ)^{28}Al	1779.65	2.23e-03	1.19e+00	2.23e-03	2415	6.87e+03
Soil_long	Channel0					

Table B.1: Table of the fitted peaks within the background-corrected spectra.

Sample/ Reaction	Energy (keV)	E_{err}	σ	σ_{err}	peak area	peak$_{err}$
^{56}Fe(n,γ)^{56}Mn	847.18	9.18e-03	1.14e+00	9.17e-03	1639	1.42e+04
^{27}Al(n,γ)^{28}Al	1779.35	3.28e-03	1.06e+00	3.29e-03	847	1.58e+03
^{56}Fe(n,γ)^{56}Mn	1810.79	7.92e-02	1.16e+00	7.92e-02	168	1.25e+03
Soil_long	Channel1					
^{56}Fe(n,γ)^{56}Mn	847.20	5.14e-03	8.59e-01	4.96e-03	764	3.01e+03
^{27}Al(n,γ)^{28}Al	1779.61	9.35e-03	1.42e+00	9.35e-03	451	7.08e+02
^{56}Fe(n,γ)^{56}Mn	1811.08	1.13e-01	1.45e+00	1.13e-01	139	7.74e+02